UNIVERSITY OF CALIFORNIA, MERCED

UNDERSTANDING CONTACT AT THE NANOSCALE USING MOLECULAR DYNAMICS SIMULATIONS

by

Rimei Chen

A dissertation submitted in partial satisfaction of the
requirements for the degree of
Doctor of Philosophy

In

Mechanical Engineering

Committee in charge:
Professor Ashlie Martini, Advisor
Professor Mehmet Z. Baykara
Professor Min Hwan Lee
Professor Tao Ye

This dissertation of Rimei Chen is approved, and it is acceptable in quality and form for publication on microfilm and electronically:

Professor Ashlie Martini, Advisor	Date
Professor Mehmet Z. Baykara	Date
Professor Min Hwan Lee	Date
Professor Tao Ye	Date

University of California, Merced

2020

Table of Contents

List of Figures

Acknowledgement

I would like to express my special appreciation to my advisor Professor Ashlie Martini for her guidance. She is professional, considerate, and brilliant. No words can describe how much I appreciate and how grateful I am for all her support and help.

I would like to thank my committee members, Professor Mehmet Z. Baykara, Professor Min Hwan Lee, and Professor Tao Ye for serving as my committee and provide helpful comments and suggestions on my dissertation.

I would like to thank my family, my dad Liuwen Chen and my mom Xianzhen Tang. Without their support, I cannot finish my Ph. D. I am really sorry that I won't be able to be there when they need me.

I would like to thank our collaborators Professor Tevis Jacobs and Dr. Sai Bharadwaj Vishnubhotla for their knowledge and responsibilities.

I would like to thank everyone in Martini Research Group: Dr. Xiaoli Hu, Azhar Vellore, Dr. Michelle Len, Arash Khajeh, Mohammad R. Vazirisereshk, Karen Mohammadtabar, Pawan Panwar, Sergio Romero Garcia, Monica Ferrera, Daniel Sanchez Garrido, Quanpeng Yang, Fakhrul Hasan Bhuiyan, Andrew Velasquez, Ting Liu, Xiaoyun Fan, Ingrid Padilla Espinosa, Brian Martin-Gutierrez. They are the best and I really enjoy working with them.

I would like to thank the support from Dr. Arben Jusufi, Dr. Alan Schilowitz, and Dr. Andrew R. Konicek at ExxonMobil.

I would like to thank all my friends for their supports and accompany: Dr. Qin Ma, Dr. Xiao Li, Dr. Yiping Guo, Dr. Yang Ju, Dr. Xi Chen, Yujing Ma, Haolin liang, Shangjie Ma etc. They made my road to Ph. D. not alone and full of laugh.

Thank you all. Life is a struggle, and we need to learn to enjoy it. I am enjoying it and hope you are too.

Curriculum Vita

EDUCATION

- Ph.D. in Mechanical Engineering, University of California Merced (Merced, CA, US), 2020 (expected)
- M.S. in Mechanical Engineering, University of Hawaii at Mānoa (Honolulu, HI, US), 2014
- B.S. in Mechanical Engineering, University of Science and Technology of China (Hefei, China), 2012

RESEARCH TECHNIQUES

- **Modelling**: Classical and reactive force fields, materials properties of semiconductor materials, metal, metal oxides, transition metal dichalcogenides.
- **Experimental techniques**: Atomic force microscopy, scanning electron and transmission electron microscopy, Langmuir–Blodgett trough.
- **Programming**: Python, C, MATLAB, Bash, LabView, LaTeX.
- **Software**: LAMMPS, OVITO, VMD, Quantum ATK, Origin, AutoCAD, SolidWorks, ImageJ, Notion, Teams.

PROJECTS

Fundamental pathways of MoS2 formation using reactive molecular dynamics simulations
Collaboration with Corporate Strategic Research at ExxonMobil (12/2018 - present)

- Modified an empirical force field to capture the crystallization of MoS_2 and investigated the thermodynamic and kinetic contributions to MoS_2 formation. The results suggested optimized conditions for MoS_2 synthesis and avenues for tuning MoS_2 properties for engineering applications.

Electronic conduction at the nanoscale: metallic contacts and effect of native oxide
Collaboration with University of Pittsburgh (08/2015 - present)

- Developed a new approach to approximating conductance in a molecular dynamics simulation and demonstrated failure of conventional electronic transport theories for ultra-thin oxides. Novel mechanism was proposed to describe conduction at the nanoscale. This has significant implications for conductive AFM and nanodevices.

Adhesion, deformation, and area of nanoscale contacts

- Discovered the load dependence of work of adhesion, contrary to the assumptions of continuum contact mechanics theories. This finding has significant implications for the fields of nanolithography, nanomanufacturing and probe-based microscopy.

SELECTED PUBLICATIONS

- Chen, R., Konicek, A., Jusufi, A., Kliewer. C.E., Jaishankar. A., Schilowitz. A., Martini, A. Limiting domain size of MoS_2: effects of stoichiometry and oxygen. *Journal of Physical Chemistry C* (accepted)
- Chen, R., Jusufi, A., Schilowitz, A. and Martini, A., 2020. Formation of MoS2 from elemental Mo and S using reactive molecular dynamics simulations. *Journal of Vacuum Science & Technology A: Vacuum, Surfaces, and Films*, *38*(2), p. 022201.

- Chen, R., Vishnubhotla, S.B., Khanal, S.R., Jacobs, T.D. and Martini, A., 2020. Quantifying the pressure-dependence of work of adhesion in silicon–diamond contacts. *Applied Physics Letters*, *116*(5), p. 051602.
- Vishnubhotla, S.B., Chen, R. *, Khanal, S.R., Hu, X., Martini, A. and Jacobs, T.D., 2019. Matching atomistic simulations and in situ experiments to investigate the mechanics of nanoscale contact. *Tribology Letters*, *67*(3), p. 97. (*indicates equal contribution, Selected as a Featured Article in the STLE Newsletter)
- Chen, R., Vishnubhotla, S.B., Jacobs, T.D. and Martini, A., 2019. Simulations of the effect of an oxide on contact area measurements from conductive atomic force microscopy. *Nanoscale*, 11(3), pp. 1029-1036.
- Vishnubhotla, S.B., Chen, R., Khanal, S.R., Li, J., Stach, E.A., Martini, A. and Jacobs, T.D., 2018. Quantitative measurement of contact area and electron transport across platinum nanocontacts for scanning probe microscopy and electrical nanodevices. *Nanotechnology*, 30(4), p. 045705.
- Vishnubhotla, S.B., Chen, R., Khanal, S.R., Martini, A. and Jacobs, T.D., 2018. Understanding contact between platinum nanocontacts at low loads: The effect of reversible plasticity. *Nanotechnology*, 30(3), p. 035704.
- Zuo, Y.Y., Chen, R., Wang, X., Yang, J., Policova, Z. and Neumann, A.W., 2016. Phase Transitions in Dipalmitoylphosphatidylcholine Monolayers. *Langmuir*, 32(33), pp. 8501-8506.

PRESENTATIONS

- Oral Presentation - 2019 STLE Tribology Frontiers Conference, Chicago, IL (10/2019)
- Invited talk - ExxonMobil Research and Engineering Company, Annandale, NJ (07/2019)
- Oral Presentation - 2019 STLE Northern California Section Meeting, Richmond, CA (05/2019)
- Student Poster - 2018 STLE Tribology Frontiers Conference Chicago, IL (10/2018)
- Oral Presentation and Student Poster - STLE 72nd Annual Meeting & Exhibition, Atlanta, GA (05/2017)
- Student Poster - 2016 STLE Tribology Frontiers Conference, Chicago, IL (11/2016)
- Student Poster - STLE 71st Annual Meeting & Exhibition, Denver, Co (05/2016)
- Student Poster - 2015 STLE Tribology Frontiers Conference, Chicago, IL (10/2015)

AWARDS

- UC Merced, Bobcat Fellowship (2016, 2020)
- STLE Northern California Section Research Scholarship (2019)
- STLE Tribology Frontiers Conference Student Poster Gold Award (2018)
- UC Merced, Department of Mechanical Engineering, Travel Fellowship (2016, 2018, 2019)
- STLE 71st Annual Meeting & Exhibition Student Poster Gold Award (2016)

UNDERSTANDING CONTACT AT THE NANOSCALE USING MOLECULAR DYNAMICS SIMULATIONS

Rimei Chen, Ph.D.
University of California, Merced, 2020
Advisor: Professor Ashlie Marini

Nanoscale contacts between materials are found in advanced technologies from nanomanufacturing to nanodevices to scanning probe microscopy. These applications require quantitative understanding of the nanoscale contact properties, such as contact area and adhesion. Continuum mechanics models are extensively used to describe and predict the behavior of such contacts, but are based on assumptions that may not hold true at the nanoscale. Additionally, the buried nature of the contact interface makes direct measurement of nanocontact a challenge. Alternatively, molecular dynamics (MD) simulations provide atomic details of the contact interface and can be used to investigate contact at the nanoscale. Here, physically realistic models of nanoscale contact were created with identically matched materials, geometry, crystallographic orientation, degree of amorphization, adhesion and loading conditions. The contact area was then computed from the positions and interactions of atoms. The results demonstrated that significant variation in the value of contact area can be obtained, depending on the technique used to determine it. Next, contact area from MD simulations was compared with predictions from electron transport theories. Electron transport theories were shown to underpredict the contact area by more than an order of magnitude. This low conductance of the nanocontact could not be explained by electron scattering off of defects, and was instead attributed to approximately a monolayer of insulating oxide on the contact surfaces. The effect of native oxide on contact area measurements was further investigated using a newly developed method to approximate conductance based on the distance between atoms in channels across the contact. Then, we compared the contact area calculated with ballistic transport and tunneling theories to that obtained using the known positions of atoms in the contact. The difference was small for very thin (<0.1 nm) or thick (>1.0 nm) oxides, where ballistic transport and tunneling theories work well; however, the difference was significant for oxides between these limits, which is expected to be the case in many practical applications. The prediction of contact area from continuum mechanics models also relies on accurate knowledge of the work of adhesion between the surfaces. An important assumption in these models is that the work of adhesion is constant for a given pair of materials. Our results challenge this assumption, instead showing a significant increase in work of adhesion with increasing pressure, and analyses suggest the presence of stress-driven chemical reactions in the contact. Overall, this research defined and computed contact properties using MD simulations and the results demonstrated the limits of empirical models, including continuum theories and electron transport theories, to describe contact at the nanoscale.

Chapter 1 Introduction

1.1 Contact at the nanoscale

As devices and manufacturing technologies shrink to the nanoscale, there is a growing need to understand, predict, and control the behavior of small-scale contacting interfaces. Examples of this need stem from nanomanufacturing, materials characterization, and nanodevices. For example, in tip-based nanomanufacturing [1, 2] and in micro-transfer printing of quantum dots [3], the behavior of the nanocontact determines reliability and precision. In the vast array of scanning probe microscopy techniques [4, 5], the contact size and properties determine both the resolution of the technique and the accuracy of models applied for quantitative analysis. Finally, for nanoscale switches and actuators [6, 7], the mechanical and transport properties of the contact determine functionality and lifetime of the device.

Atomic force microscopy (AFM) has commonly been used to study the contact at the nanoscale [8, 9]. Figure 1.1a shows a schematic of an AFM setup. The AFM setup contains a sharp tip and the interaction between the tip and the substrate is measured from the deflection of the tip. Typically, the AFM tip has a radius in a range of 10 to 100 nm. The contact between the tip and substrate represents a single asperity contact. The interaction force between the tip and the substrate can be measured with nN resolution. Accordingly, the interaction force of the contact process (as the tip approaches and retracts from the subtract) can be obtained as a function of their separation (see Figure 1.1b). Consequently, the properties of the contact between the tip and substrate can be investigated from the geometry and the interaction force. The contact properties can be obtained using continuum contact mechanics models (Section 1.2), direct and indirect experimental measurements (Section 1.3), or molecular dynamics (MD) simulation (Section 1.4).

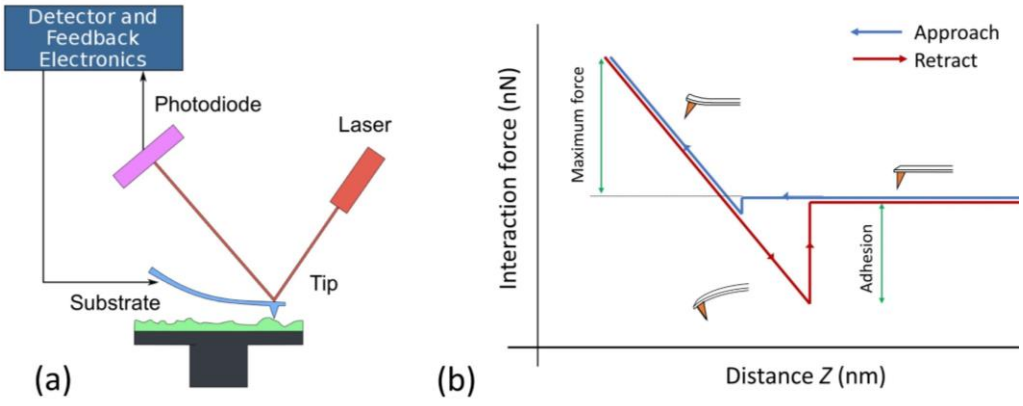

Figure 1.1 (a) A schematic of an AFM where contains a sharp tip and a flat substrate. This image is from Ref. [10] (b) A reprehensive force distance curve as the tip approach and retract from the substrate.

1.2 Overview of application of continuum contact mechanics at the nanoscale

1.2.1 Continuum contact mechanics models

By combining the geometry and mechanical properties of the two contacting bodies, continuum contact mechanics models could be applied to predict the contact behavior. The well-known Hertz model [11] describes contact between two spheres or a sphere on a flat surface, where the contact radius could be predicted by the geometry and stiffness of the contact bodies, as well as the applied load F_{app}. The form of the Hertz model is given by:

$$a_{Hertz} = \left(\frac{3F_{app}R_{eff}}{4E_{eff}}\right)^{\frac{1}{3}} \tag{1.1}$$

Where R_{eff} is the effect radius of the two contact bodies and is defined as $R_{eff} = \left(\frac{1}{R_1} + \frac{1}{R_2}\right)$. E_{eff} is the effective modulus and is defined as $E_{\text{eff}} = \left[\frac{(1-\nu_1^2)}{E_1} + \frac{(1-\nu_2^2)}{E_2}\right]^{-1}$, where E and ν are the elastic modulus and Poisson ratio of the two contact bodies. The Hertz model assumes the contact bodies are homogeneous, isotropic, smooth, and exhibit elastic behavior. Additionally, adhesive force is neglected in Hertz model. However, at the nanoscale, the adhesive force become dominant as the surface-to-volume ratios increase. The extensions of the Hertz model, such as Derjaguin–Müller–Toporov (DMT) [12] and Johnson–Kendall–Roberts (JKR) [13] are used to describe contacts when adhesive force is under consideration. In general, DMT is applicable for stiffer materials with weaker and longer-range adhesive interactions, while JKR is applicable to more compliant asperities with stronger and shorter-range adhesion. The mathematical aspects of and transition cases between DMT and JKR have been described previously. Using these spherical contact models, the contact radii calculated by DMT and JKR, respectively, are given by:

$$a_{DMT} = \left(\frac{3(F_{app}+F_{adh})R_{eff}}{4E_{eff}}\right)^{\frac{1}{3}} \tag{1.2}$$

$$a_{JKR} = \left\{\frac{3R_{eff}}{4E_{eff}}\left[F_{app} + 3W_{adh}\pi R_{eff} + \sqrt{6W_{adh}\pi R_{eff}F_{app} + \left(3W_{adh}\pi R_{eff}\right)^2}\right]\right\}^{\frac{1}{3}} \tag{1.3}$$

where F_{adh} is the adhesive force. W_{adh} is the work of adhesion between the contact bodies.

The work of adhesion W_{adh} can be calculated from the adhesive force F_{adh} as:

$$W_{\text{adh}} = F_{\text{adh}}/(\chi\pi R) \tag{1.4}$$

where $\chi = 2$ for DMT and $\chi = 1.5$ for JKR. First Tabor [14] and later Maugis [8] showed that the DMT and JKR are two extreme limits for describing a continuum of contact behavior. The transition region between the limits can be characterized by a dimensionless transition parameter [14, 15] (μ_T or λ) which is the ratio of elastic deformation to the length-scale of surface forces. In the transition region, Maugis [15] provided expressions for deformation and contact area as functions of applied load. These equations were simplified by Carpick *et al* [16] to present a numerical analysis for determining the contact area in the transition region. Similar numerical analysis was extended for determining deformation in the transition region [17].

1.2.2 Application of continuum mechanics models at the nanoscale

Nanoscale contact area is most commonly predicted using continuum mechanics models (as reviewed in Ref. [18]) due to their ease of use and closed-form predictions for contact radius. There are numerous AFM investigations where measured data has been accurately fit by applying continuum contact mechanics, as discussed in Ref. [16, 19–21]. Carpick et al. used a Pt-coated tip to contact with a mica surface and found that continuum models and their extended models could be used to describe the nanocontacts [19, 21]. Enachescu et al. performed a nanocontact between a hydrogen-terminated diamond(111) tip and a tungsten carbide surface in ultrahigh vacuum and found the area-load relation of this extremely hard single asperity contact could be described by the DMT continuum mechanics model [20]. However, these experiments were conducted in extremely conditions for certain materials and required geometry assumptions from the contact bodies. In most engineering applications, these conditions may not be achieved and therefore, the continuum contact mechanics models may not hold true. For example, capillary effects [22] or viscoelasticity in soft materials [23, 24] may cause adhesion hysteresis [25] in the area-load relation. This hysteresis between approaching and separating could not be captured by the continuum mechanics models. Therefore, a more general limit of these continuum contact mechanics models at the nanoscale is required to predict the contact properties for many engineering applications.

1.3 Experimental methods for measuring the area and adhesion of nanocontacts

The contact interface is buried under two contact bodies, which makes accurate measurement of contact area in experiments a challenge. The contact area can be determined using two approaches: (1) indirect measurement, where the contact area computed from one or more other functional properties of the contact; (2) direct measurement, where the contact area measured from the real-time imaging of the contact.

1.3.1 Indirect methods for measuring nanoscale contact area

Contact area can be determined indirectly by measuring functional properties of a contact, e.g. electrical and thermal contact resistance [26, 27], normal contact stiffness [28], lateral stiffness and friction forces [29].

The contact area can be estimated through the contact resistance using the electron transport theories including ballistic and tunneling models. Several investigations have measured the resistance through the tip/substrate contact using scanning probe microscopy and computed the contact area using the ballistic model. One investigation showed qualitatively the effect of the materials contribution to resistance. More recently, a method was demonstrated to quantitatively treat the contribution of an oxide using the tunneling model. Fitting the model to measured data enables the calculation of what the author call an “electrical contact area”. Measuring the contact area from thermal contact resistance exhibits similar concept as from the electrical contact resistance, except that heat can be carried by electrons and phonons which will have different mean free paths and different

scattering behavior. Gotsmann and Lantz have measured thermal contact resistance between a flattened silicon probe tip and a tetrahedral amorphous carbon surface as a function of load and tip size [11]. The results are fit using a model that assumes quantized thermal transport through individual atomic regions, such that the measured thermal conductance scales with the true area of contact.

The stiffness of the AFM contact is a function of the mechanical properties of the materials in contact, and also of the contact area. Prior investigations have assumed smooth spheres in linear elastic contact and applied the Hertz model to describe the contact stiffness, where the stiffness is directly proportional to the contact radius. It has been shown this model applies to all smooth, rigid, rotationally symmetric bodies in elastic contact and a correction factor required for larger loads and other prismatic bodies.

Measurements of lateral forces have also been used as an indirect measure of contact. For a sticking contact, for which sliding has not yet initiated, the lateral contact stiffness can be computed as the derivative of the lateral force-displacement curve and is proportional to the contact radius for a Hertzian contact. This model has been applied to scanning probe microscopy measurements of lateral stiffness to determine contact area. For sliding contacts, the behavior is governed by sliding friction and dissipative force, so the concept of lateral stiffness no longer applies. Here it is often assumed that friction force is directly proportional to the true contact according to the originally proposed by Bowden and Tabor, with a constant of proportionality that equal to the shear stress of the interface. The contact area has been directly extracted from quantitative sliding friction tests.

These indirect measurements of contact area using contact properties are all required a model to extract the contact area from the measurements. These models rely on significant assumptions about the materials, properties, and shape of the contact. Many of these methods assume that the bodies in contact have the shape of a smooth well-defined geometric function (e.g., sphere, or rotationally-symmetric power-law, etc.), and therefore the area of contact is a single continuous surface. However, surface roughness on either or both bodies can contribute to the formation of a multi-asperity contact, in which case the direct application of the above models is not straightforward.

1.3.2 Direct methods for measuring nanoscale contact area

To directly measure contact area, researchers have conducted the AFM experiments inside of a transmitted electron microscope (TEM) [30, 31], which provides atomic resolution of the contact bodies, and so called *in situ* TEM technique. Figure 1.2 shows (a) an image of this *in situ* setup and (b) a TEM image of an AFM tip. The *in situ* TEM technique is able to directly observe instantaneous contact behavior. However, since the contact interface is buried in between the two contact bodies, the properties and atomic details of this buried surface are still unknown.

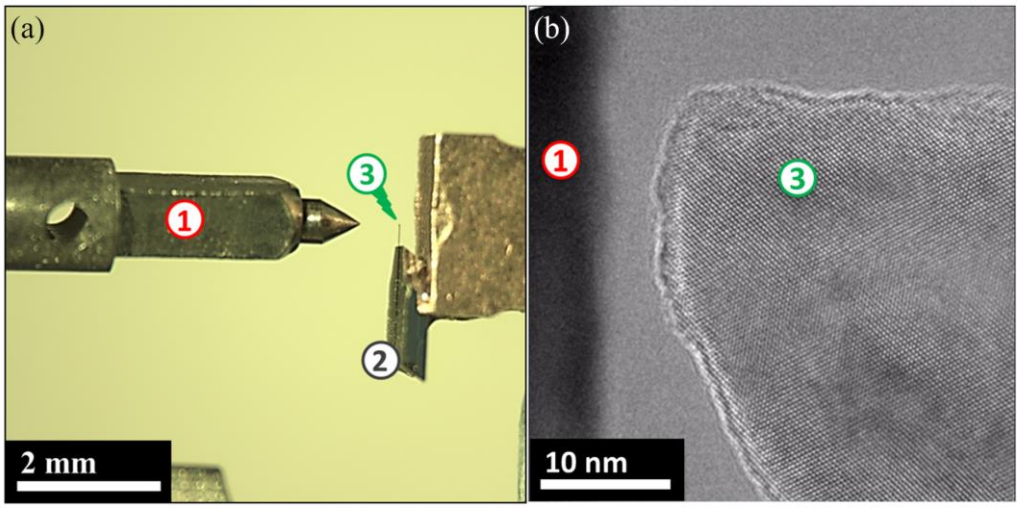

Figure 1.2 (a) Optical and (b) TEM images of the experimental setup enabling an in situ contact test inside of a transmission electron microscope. A flat diamond indenter (1) is opposite an AFM chip (2), such that it can be brought into contact with the nanoscale tip (3). This experiment image is provided by Professor Tevis Jacobs' research group at the University of Pittsburgh.

In situ TEM technique enables direct measurement of contact area. *In situ* TEM experiments designed specifically to study nanocontacts were used to investigate dissimilar contacts that do not undergo spontaneous welding [32]. This apparatus was used to quantitatively characterize the out-of-contact geometry of the AFM tip, as well as to measure the corresponding adhesion [30, 33, 34], wear [32], and electrical [35] properties. Such studies show that, in the general case, there is not fusion of the opposing bodies, but instead the original interface remains distinct. In all cases, *in situ* TEM provides a way to measure the geometry of the bodies, as well as their structure, and composition. During contact, side-view images can be used to compute the diameter of the contact and, under certain assumptions, its contact area.

Direct assessment of contact area eliminates the need to assume a functional dependence of a measured property on contact area (which requires significant assumptions about the shape, size, composition, and structure of the bodies in contact). However, the *in situ* experiments add their own constraints and assumptions. First, the measurements are typically slow and time- and resource-intensive, which precludes the conduction of a very large number of repetitions for statistical analysis. Second, to be imaged in the TEM, the samples must be thin enough to be electron transparent (less than approximately 100 nm in thickness) and conductive enough to avoid significant charge build-up under the electron beam. Third, the energetic electron beam used for imaging can inadvertently change the behavior of the materials under study: changing their mechanical properties, or decomposing or contaminating the material. Fourth, for non-welding contacts, the measurement of the contact diameter is limited by imaging resolution and TEM artifacts, as well as by apparent overlap between the contacting bodies due to slight out-of-plane

shifts. Fifth, only a 2-D projection of the contact is visible in the TEM and the ability to tilt is typically limited. Therefore, assumptions must be made about the shape and extent of the contact size in the direction parallel to the imaging beam.

1.3.3 Measuring work of adhesion at the nanoscale

The primary factors governing adhesion between bodies are the fundamental physical interactions between the materials and the geometry (global and local) of the surfaces in contact. The first factor includes the atomic-scale interactions such as van der Waals attraction, electrostatic interactions, and atomic bonding and is described by the work of adhesion W_{adh}, which is the energy required per unit area to separate flat surfaces of the two materials. In terms of surface energy γ of the two materials, $W_{adh} = \gamma_1 + \gamma_2 - \gamma_{12} = 2\gamma$ (for a self-mated contact). Just two years after London's theory of van der Waals interactions, Bradley [36] demonstrated the effect of geometry on adhesion when he showed that the adhesive force between two identical rigid spheres of the same material can be described as $F_{adh} = 2\pi R W_{adh}$. To compute the work of adhesion from the adhesive force, pull-off test are typically performed using atomic force microscopy [37]. The interaction force is captured during the tip approaching and retraction processes where the minimum attractive force is the adhesive force. This method requires the assumptions of continuum contact mechanics are applicable at the nanoscale and that the work of adhesive is a constant and only depends on the surfaces.

1.4 Molecular dynamics simulations of nanocontacts

An alternative to continuum models is atomistic simulations. Molecular dynamics (MD) simulation, which is based on Newton's second law, has been introduced to complement experimental studies of contact at the nanoscale. In MD simulation, properties such as the position, or force of each atom in the model system can be calculated, which provide atomic details of the contact behaviors. Additionally, MD simulation is able to flexibly and precisely control the contact conditions, like temperature, oxidation of the contact surfaces, and degree of amorphization of contact materials, where those conditions are difficult to control in the experiment. Many MD studies, including those reported in this proposal, are performed using Large-scale atomic/molecular massively parallel simulator (LAMMPS) [71] , which is a molecular dynamics program from Sandia National Laboratories.

MD simulations have been used to model contacts between a curved tip and a flat substrate. Physical representative models with tip radii from 10 to 100 nm have been simulated to investigate the effects of tip radius and the contact properties by mimicking experiment conditions [38–41]. To evaluate contact properties (e.g. contact area) using MD simulations, contact area is calculated based on the position of each atom. Contact has been defined based on the distance [42, 46, 47], or the interaction force [48, 49] between atoms. Cheng et al. used contact atoms that resulted in 95% of the contact pressure to compute the contact area and found this contact area was 2-4 folds larger than the Hertz predictions [48, 49]. Mo et al. compared the atomistic contact area to the apparent contact area with a convex hull to enclose contact atoms and found the atomistic contact area was suitable for

the further friction properties study. A review of the contact area measurement methods can be found in Ref. [50]. Contact area can be measured from varying definition and methods. The results depend on the measurement technique and lack of validation.

Simulations have also been used to characterized contact area measured through conductance (see section 1.3.1). However, some investigations suggest the failure of electrical transport theories to describe transport through gold nanocontacts [51] with lower conductance than expected. This low conductance might due to the insulating layer on the contact surfaces that cannot be observed or characterized from experimental technique. Atomistic simulations can provide some insight into the effect of such insulating layers because they explicitly model the size and morphology of the contact. Density functional theory or *ab initio* molecular dynamics enable the direct calculation of conduction [52–56], but are limited to very small size scales and so cannot capture the deformation at technologically relevant size scales. Alternatively, there have been extensions of classical MD developed that enable calculation of conduction [41, 57]. This approach does not differentiate between atoms which limits the study of insulating films. A recent study by Yang, *et al.* [58] used classical MD simulations to understand the effect of small amounts of adsorbates on conduction in Pt nanoasperities for nanoelectromechanical switches. This study considered current flow through direct metal-metal contact and did not attempt to include contributions due to tunneling, which may play a significant role in the case where one or more of the metals has at least a full monolayer of oxide coverage. Accordingly, the study of contact area through conductance requires methods to estimate conductance in MD simulations with insulating films on the contact surfaces.

Further, simulations provide atomic surface roughness and covalent bonding information to study the origins of adhesion. Molecular dynamics simulations using silicon probes and diamond substrates revealed that adhesion is impacted by plastic rearrangements in the probe during sliding, i.e., smoothing, and by the presence of probe-substrate covalent bonds at the time of probe pullback. [59] Furthermore, the simulations showed that hydrogen termination of the diamond, applied load, sliding distance, and initial probe roughness all impact the simulated adhesion. Another recent study [60] examined the contact size of a silicon probe on diamond during loading and unloading and showed how the loading data could only be fit using a value of work of adhesion that increased with load up to the maximum force that was applied. However, these studies only focused on work of adhesion with a constant or static load. Potential changes in the work of adhesion with applied load have not been examined.

Some MD simulations have suggested that contact mechanics may be applied when atomic-scale surface roughness is considered in the model [42] or for modifications of the theories, such as thin-coating contact mechanics [38, 43]. However, Luan and Robbins have found that atomic roughness at the surface resulted in deviations of the pressure distribution with models exhibited the same tip radii but with different surface features [44, 45]. This deviation cannot be predicted by continuum contact mechanics models. Therefore, the applicability of the continuum mechanics models at the nanoscale is still unclear.

1.5 Dissertation outline

Previous studies have suggested that contact mechanics may be applied [12, 21, 23, 31, 32] or may break down at the atomic scale [40, 44, 45, 61, 62]. However, the experiments and simulations were conducted under specific conditions and were only for certain materials. Further, in simulations, previous research has shown different methods to compute the contact area can lead to different results [47]. Many previous simulation results lack validation and are limited by the ambiguity of the definition of the contact at the nanoscale. Therefore, investigation of the applicability of the continuum contact mechanics models and validation of contact area calculations in simulations are required.

In this proposal, our goal is to define contact, develop a solid method to calculate contact area at the nanoscale and reveal the fundamental mechanisms of work of adhesion. To achieve this goal, in chapter 2, we use molecular dynamics simulations to develop a physically realistic nanocontact model and calculate the contact area with different methods. The contact area from simulations is then compared with direct experiment measurements and continuum contact mechanics predictions. We further explore the load dependence of the contact area for this nanocontact model to analyze the applicability of the continuum contact models. In chapter 3, we use conductance as an alternative way to measure or verify the contact area measurement. First, the contact area is measured using *in situ* experiments and simulations with the methods developed in chapter 2. The results are then compared with the contact area estimated from conductance and electron transport theories. In chapter 4, the effect of native oxides on contact area determined from conductance is discussed and the applicability of electron transport theories for contacts with thin oxides are evaluated. In chapter 5, the pressure-dependence of work of adhesion is studied using simulation and experiments. Finally, we propose research on: (1) general limits of continuum contact mechanics models regarding tip geometry and contact pressure; (2) the origin of load dependent adhesion at the nanoscale.

Chapter 2 Contact area measurement at nanocontacts

2.1 Introduction

Nanoscale contact area is most commonly predicted using continuum contact mechanics models. Contact mechanics models are easy to apply and make closed form predictions for contact radius, but their validity at the nanoscale has been questioned [44, 45, 63, 64], especially due to the effects of atomic-scale roughness. Alternatively, contact area can be measured in one of three ways [50]: it is directly measured using *in situ* observation; it is computed from indirect properties, such as by measuring current flow and applying electronic transport theories; or it is extracted from an atomistic simulation. Each of these approaches has its assumptions and limitations. First, direct observation can be performed with atomic resolution [65], but this approach typically lacks the load resolution to measure the nanonewton-scale loads that are relevant to nanocontacts. Second, electronic transport models are extremely well validated in highly controlled environments [66] (such as in scanning tunneling microscopy or in mechanically controllable break junctions), but their accuracy can be reduced for real-world nanocontacts operating in an ambient environment due to factors such as oxide and contamination. Finally, atomistic simulations provide atomically resolved detail into the contacting interface, but the value of contact area can depend on how it is measured [48] and the generalizability of results to real-world systems is not always clear.

In this study, we used molecular dynamics simulation to model a physically realistic contact between a flat diamond indenter and a sharp silicon tip. The simulations were designed to faithfully reproduce the key features of AFM experiments so that the two can be used together to compare the contact area of the same nanoscale contact. Different methods were employed to measure the contact area. Our goal for this chapter is to compare the contact area calculated using different techniques and test the applicability of continuum contact models.

2.2 Methods

Molecular dynamics simulation was used to model a physical realistic contact between a silicon tip and a diamond substrate. The shape and material composition of tip were obtained from transmitted electron microscopy (TEM) images, courtesy Dr. Tevis Jacobs at the University of Pittsburgh. According to the TEM imaging, the tip was composed of crystalline silicon with an amorphous region at the perimeter of its apex. The high-resolution TEM image of the tip in Figure 2.1a was traced to extract the 2D profiles of both the crystalline and amorphous regions. The method of disks [67] was used to create 3D surfaces for the tip shape, under that the assumption that the 2D profile is representative of the tip shape in all orientations. This assumption is supported by previous work on sliding wear of silicon. For example, Ref. [68] compares side-view TEM images to the results of numerical 3D tip reconstruction from AFM scans; the results show similar radii in all orientations. Further, even a difference of 5% in tip radii between in-plane and out-of-plane orientations would cause an error of less than 1% in computed results [69].

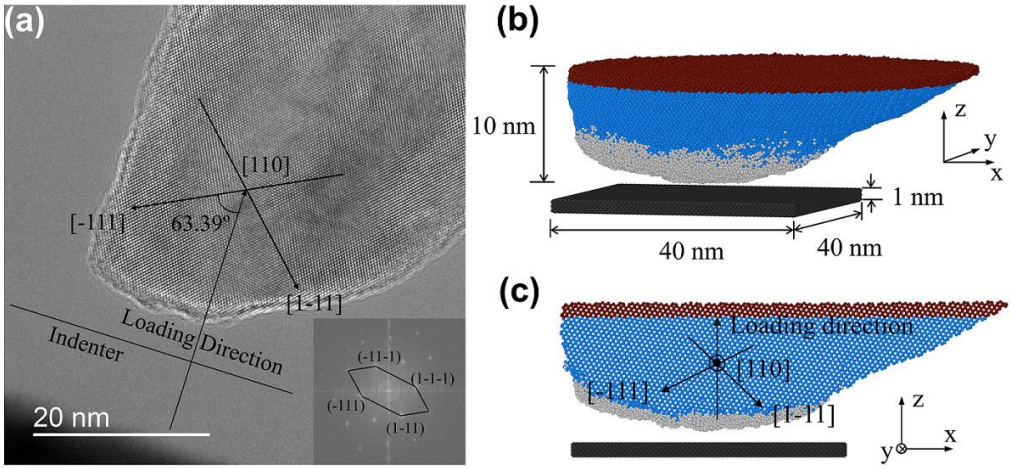

Figure 2.1 A high-resolution TEM image (a) of the AFM tip is shown with crystallographic and loading directions labeled. The inset image shows the fast Fourier transform (FFT) pattern of the corresponding TEM image. This experiment image is provided by Professor Tevis Jacobs' research group in University of Pittsburgh. The atomistic model is shown in perspective (b) and cross-sectional (c) views. Sphere color represents atom type, where: blue is crystalline silicon; silver is amorphous silicon; red is the rigid part of the tip; and black is carbon.

The crystallographic direction of the crystalline region of the tip was set based on the diffraction pattern from the TEM. The height of the tip model was 10 nm. The substrate consisted of carbon atoms in a diamond lattice and had dimensions of 40 × 40 × 1 nm in the *x*, *y*, and *z* directions respectively. The substrate atoms were held rigid for computational efficiency. According to the Hertz model, this assumption is expected to introduce differences in contact area and deformation of approximately 7% from the experiment. However, this was accepted since an accurate description of elasticity on both bodies would have required a significant increase in the simulation size. The substrate was modeled as a flat surface because the radius of curvature of the overall shape of the indenter was measured to be 1000 nm. Nanoscale roughness on the substrate was neglected because its accurate inclusion would require knowledge of the precise location of the tip contact – including in the out-of-plane direction. This cannot be identified with sufficient precision due to the finite resolution in the TEM. Fixed boundary conditions were applied in all directions.

The topmost 1 nm of the tip were treated as rigid bodies. Treating the diamond substrate as rigid will introduce an A Nosé-Hoover thermostat was applied to the 4-nm region immediately below the rigid layer to control the temperature of the system at 300 K. The remainder of the tip atoms were integrated using the NVE (constant number of atoms, volume, and energy) ensemble, which enabled the simulation to capture the dynamics of atoms in the contact interface [70]. Simulations were carried out using the molecular dynamic simulation package LAMMPS [71] with a time step of 1 fs.

There were four processes during the simulation: equilibration, loading, relaxation, and unloading. In each process, the interaction force between the tip and substrate was characterized. The interaction force was calculated as the sum of the forces on the tip atoms [40]. The tip was initially placed at a distance of 0.7 nm above the substrate. This distance was greater than the cut-off distance of the empirical potentials. Thus, there was no interaction between the tip and the substrate during the equilibration process. After the system reached stability in temperature and energy, which indicated the system was at equilibrium, a constant downward velocity of 5 m/s was applied to the rigid body of the tip. The tip moved towards the substrate until it reached the maximum force observed from experiment. After the tip reached the maximum force, it was relaxed for 0.7 ns to ensure stability in energy and force. After relaxation, the tip was retracted from the substrate at 5 m/s to simulate an unloading process. Due to realistic limitations of computation time, the loading and unloading speeds were significantly faster than experiment. However, contact mechanics models do not predict an effect of pull-off speed for hard, non-viscoelastic materials. Further, thermally-activated processes such as creep are not expected to play a significant role in the present contact.

The modified Tersoff potential [72], which is known to be able to capture accurately the mechanical properties of silicon, was employed to simulate the interactions within the silicon tip. The interactions between tip and substrate were modeled by the Lennard-Jones potential with the addition of a Buckingham potential to capture the large short-range adhesive interactions that were observed in the experiment. The Lennard-Jones potential approximated the van der Waals attraction and Pauli repulsion between the materials, and the parameters were set at $\varepsilon = 0.0024$ eV, $\sigma = 0.28$ nm [73]. The Buckingham potential was used to add an additional attractive force between the tip and the substrate [74, 75]. The Buckingham potential has the form $E = -\alpha e^{-r/\zeta}$, where α is the maximum attractive energy between two atoms, and ζ is the characteristic short-range decay length. The value of ζ was set to be 0.3 times the value of σ of the Lennard-Jones potential [74, 75]. The pull-off force increased approximately linearly with the magnitude of the parameter α, and the experimental pull-off force was reproduced in the simulation using a value of $\alpha = 3.5$ eV. This extracted Buckingham parameter α comparable to the energy of a silicon-carbon bond, which is 3.3 eV [76].

2.3 Matching interaction between simulations and experiments

To ensure that the simulations and experiments were describing the same nanocontact, it was necessary to match the adhesion strength at the interface, as quantified by the pull-off force. Figure 2.2 shows the force-vs-time data from the experiment and the simulation. The maximum force and the pull-off force from the simulation was matched with the experiment data with the maximum force and the pull-off force were 367 ± 2 nN and 457 ± 8 nN, respectively.

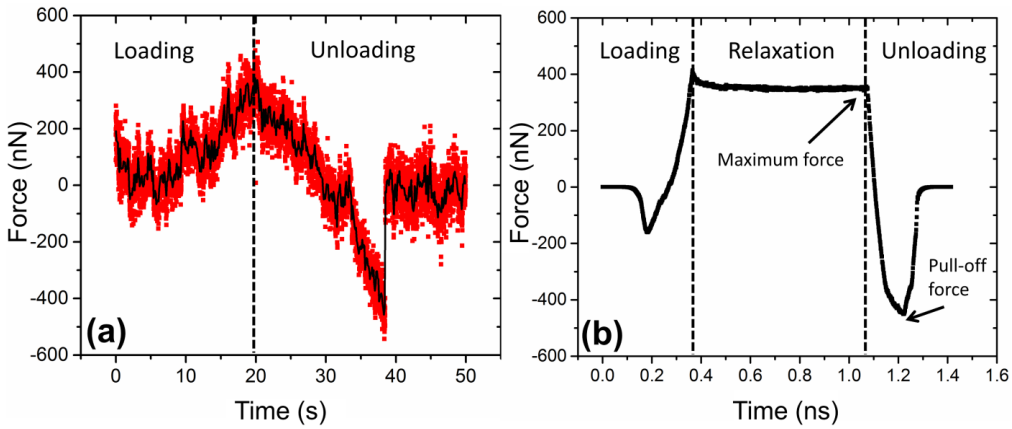

Figure 2.2 The force as a function of time from experiment (a), shown as both raw (red symbols) and downsampled (black line) data, and from simulation (b). As shown, the maximum and pull off forces are matched between experiment and simulation, while the timescales differ significantly. Experimental data is provided by Professor Tevis Jacobs' research group in University of Pittsburgh.

2.4 Geometry assumptions for continuum contact mechanics models

To be able to apply the continuum contact mechanics models, the geometry and deformation information of the tip were required. Therefore, these two steps were performed: (1) evaluate the geometry of the body to confirm a parabolic shape and measure tip radius; (2) compare the shape of the bodies before and after contact to confirm that there was no change in overall shape due to testing.

To evaluate the geometry of the bodies, the outer contour of the tip was traced using image analysis. To verify near-parabolic shape (Step 1), the traced contour was fit to a parabola of the form $z = x^2/2R$, where z is the vertical height, x is the lateral dimension, and R is the radius. To assess changes with testing (Step 2), the traced contours were compared before and after testing. Before testing, the tip radius was 20.0 ± 1.8 nm and the root-mean-square deviation from the paraboloidal shape was 0.17 nm. After testing, the tip radius was 20.7 ± 1.4 nm with an RMS deviation of 0.16 nm. While there were Angstrom-scale modifications to the tip, the tip remained paraboloidal. The geometric assessment supports the application of classical contact mechanics models.

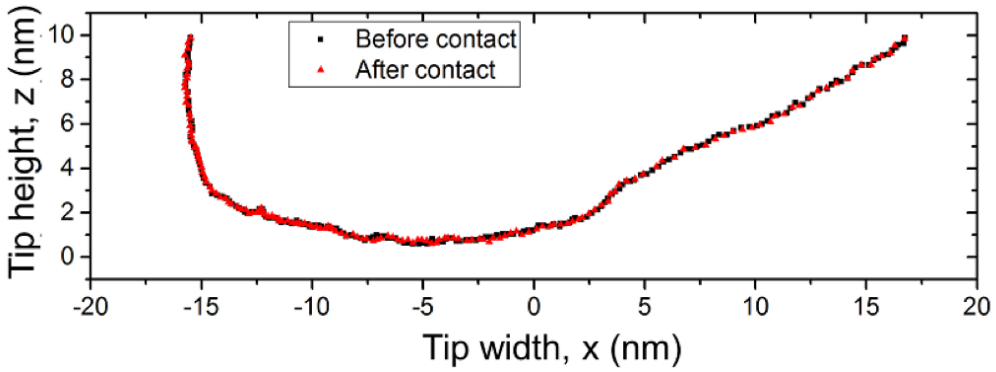

Figure 2.3 Tip profile from the simulation before and after contact. There is minimal shape change observed.

2.5 Contact area measurement at the maximum load

To demonstrate the variation in contact area calculations for a simulated contact, the area of contact at the maximum force was evaluated using a variety of different methods. These methods are discussed explicitly in Ref. [50]. In the simulation, contact area is obtained by first identifying the atoms that are 'in contact', and then convert contact atoms into contact area.

2.5.1 Contact atoms identification

There are two different methods to identify the contact atoms: (1) a distance criterion; and (2) a force criterion. The value of d_c = 0.25 nm was set as the distance at which the Si-C interatomic potential energy is a minimum [42, 46, 47]. In the force criterion, the time-averaged interaction force was calculated between each tip atom and the substrate. If the tip atom experienced a repulsive force from the substrate, this tip atom was considered to be in contact with the substrate [48, 49]. The time-averaged forces on the tip atoms were calculated over different time intervals at steady state, i.e. the observation time interval varied from 1 to 10,000 time steps. The results from both methods are shown in Figure 2.4 for the point of maximum force.

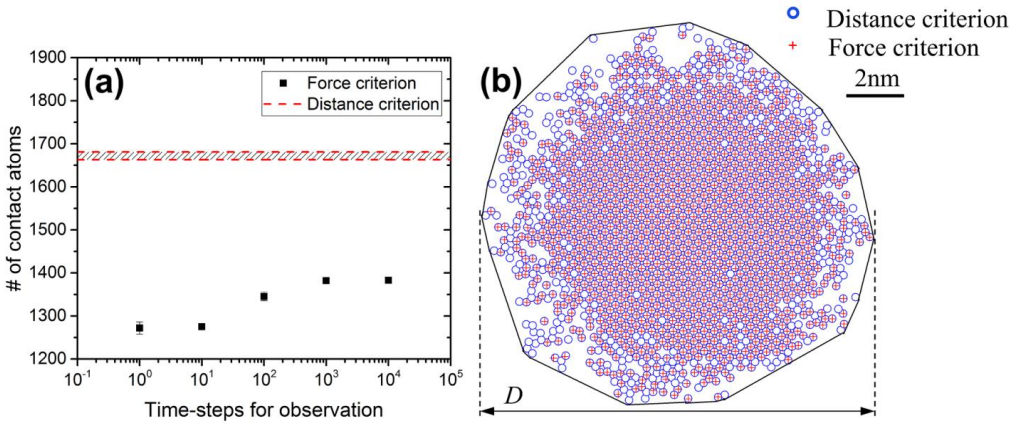

Figure 2.4 (a) Number of contact atoms at the maximum force as calculated using the distance criteria and the force criteria with increasing observation time. (b) Representative image of the contact atoms identified from the distance criterion (blue circles) and the force criterion (red crosses). The convex hull method defines the contact area enclosing the contact atoms (black outline). The side-view diameter method defines a circular contact with a diameter measured along the axis corresponding to the viewing direction of the TEM (marked as *D).*

Using the force criterion, the number of contact atoms increased with increasing force-averaging time interval and then saturated after approximately 1000 time steps. This time-dependence does not reflect physical changes in the material, but is rather attributed to thermal fluctuations and the fact that short-time fluctuations are averaged out [48, 49]. Therefore, only the longest observation period is reported in the rest of the present discussion, in accordance with Ref. [49]. Using the force criterion with the longest observation period yielded a value of 1383 ± 4 atoms. Using the distance criterion, the mean number of contact atoms was 1672 ± 9. This result is shown as a horizontal bar in Fig. 2.4(a), where the width of the bar represents the standard deviation of the data. Although results from both the force and distance criteria calculations are shown in Fig. 2.4(a), the distance criterion results are inherently time averaged and so do not depend on observation time.

2.5.2 Contact area calculations

After identifying contact atoms, the contact atoms were converted into a measurement of contact area using each of three different methods: (1) multiplying the number of contact atoms by the area of a single atom (called “atomic area method”); (2) measuring the area of a polygonal region enclosing the contact atoms (called “convex hull method”); and (3) computing the area of a circular contact described by the diameter that is measured in an orientation that corresponds to the viewing direction of the TEM (called “side-view diameter method”). These methods are illustrated in Fig. 2.4(b). Finally, to rule out the viewing orientation, contact area was measured using averaged-view diameter method

which is the average of the diameter measured from the six viewing directions (0° along the TEM view, 30°, 60°, 90° (along the x axis), 120°, and 150°). The difference between side-view diameter method and the averaged-view diameter method is 3.5%. As expected, the atomic area method yielded the smallest estimated area (73.1 ± 0.4 nm^2 and 58.8 ± 0.4 nm^2 for the distance and force criterion, respectively). The value from the convex hull method was significantly larger (131.3 ± 0.8 nm^2 and 125.6 ± 1.0 nm^2 for the distance and force criterion, respectively) because this calculation assumes continuous contact [42, 63]. Lastly, the side-view diameter method and the averaged-view diameter method, which are most similar to the area obtained from TEM images in the experiment, resulted in the largest estimated areas (132.7 ± 0.2 nm^2 and 125.9 ± 8.5 nm^2 for the force criterion, respectively).

2.6 Contact area comparisons with different computed methods

For comparison, at the maximum force, the contact area obtained from the TEM image was 149.8 ± 55.4 nm^2, where the uncertainty is due to vibration of the indenter. The DMT, JKR and the Maugis-Dugdale theories predict values of 69.1 ± 4.7 nm^2, 142.2 ± 9.6 nm^2, and 122.8 ± 7.6 nm^2, respectively. These are using the tip radii and works of adhesion, and an effective modulus of 126.9 GPa. This effective modulus was computed as $E_{eff} = \left[\frac{(1-\upsilon_1^2)}{E_1} + \frac{(1-\upsilon_2^2)}{E_2}\right]^{-1}$, where the first material is [1 0 0] diamond (E = 1050.0 GPa, ν = 0.1) [77] and the second material is the silicon, oriented along the loading direction. The latter properties were E = 132.8 GPa and ν = 0.28, which were obtained from elastic constants C_{11} = 165.6 GPa, C_{12} = 63.9 GPa, C_{44} = 79.5 GPa [78] and a loading direction of [2 $\bar{2}$ 19].

The results of all contact area calculations are shown in Fig. 2.5. The variation in contact area shown for each of the three continuum mechanics models reflects the uncertainty in the radius fit to the pre-test TEM images of the tip. Variation in the viewable diameter contact area corresponds to resolution of the in-contact TEM images. Comparison of all approaches and the uncertainly associated with each demonstrates the wide range in possible measured values, even for a simulated contact with known atomic positions. This underscores the complexity of defining an accurate value for contact area. It is likely that the "correct" area of contact to use will depend on the intended application. For instance, the rate of atomic-scale wear via chemical reactions will likely depend more strongly on the atomic area of contact. While the electrical transport (in the ballistic limit [79]) will likely depend more strongly on the area computed using the convex hull. For the remainder of this discussion, the viewable diameter from the TEM experiments will be compared against the averaged-view diameter method from the simulation, as these are the most directly analogous. Overall, the variability in computed values demonstrates that caution is required whenever two absolute values of contact area are compared. For a more robust analysis, the contact area must be computed at a variety of applied forces, as is done in the next sub-section.

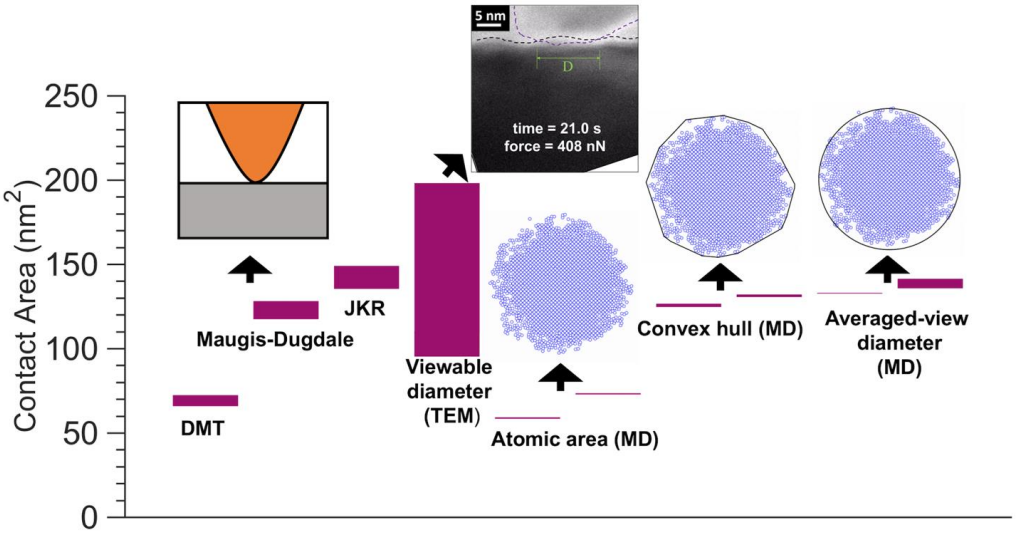

Figure 2.5 Contact area at the maximum applied force of 408 nN: as predicted by continuum contact mechanics theories; as obtained from the *in situ* high-resolution TEM video; and as calculated from the atomistic simulations using different approaches. For each of the simulation measurements, two values are shown corresponding to the force (left) and distance (right) criteria. Experimental data is provided by Professor Tevis Jacobs' research group in University of Pittsburgh.

2.7 Load dependence of the contact area

The contact area as functions of applied force is shown in Fig. 2.6. The contact area demonstrates hysteresis in behavior between the loading and unloading portions of the tests. The contact area at zero applied force is larger upon unloading by 101% as compared to the same value measured during loading. This hysteresis behavior is not predicted by continuum elastic models. While this can be a hallmark of permanent changes within the material, there is no gross shape change observed before/after testing, as shown in Fig 2.3. None of the contact mechanics models (JKR, DMT, Maugis-Dugdale) could capture the hysteresis between loading and unloading behavior; therefore, these two segments were investigated independently. The unloading curve could be accurately fit using the intermediate case of Maugis-Dugdale with an effective modulus of 98.1 GPa. The extracted best-fit value for effective modulus from the simulation is lower by 22.7% to that of the crystalline silicon.

By contrast, the Maugis-Dugdale model with the same parameters overestimated the contact area upon loading by 46%. Indeed, the loading portion of the curve could not be accurately fit for any value of E_{eff}. Therefore, the fit was retried allowing for a variable work of adhesion. Specifically, W_{adh} was allowed to vary with force, while the radius was held constant at the measured value (20.7 nm) and the effective modulus was held constant at the best-fit value (98.1 GPa) determined previously. Fig. 2.6(a) shows the measured data, alongside curves representing the Maugis-Dugdale model with varying works of adhesion. Fig. 2.6(b) shows the extracted best-fit work of adhesion at each value of the stress in the

contact. This best-fit value increases monotonically from 1.3 J/m^2, which accurately fits the contact area and force at the initial point, to 4.3 J/m^2, which fits well the contact area and force for the unloading data.

The variation between properties measured during loading and unloading has been observed in a variety of materials and is often referred to as *adhesion hysteresis* [25]. However, this effect is typically attributed to capillary effects [22] or to viscoelasticity in soft materials [23, 24], or to plasticity in hard materials.[80] By contrast, the present test used hard non-viscoelastic materials (silicon and diamond). Further, the MD simulations showed no significant shape change upon testing. In the absence of these other explanations, it appears that the hysteresis may stem from changes in the strength of the interactions across the interface as the contact is loaded. This variable work of adhesion may be explained by increased formation of bonds across the interface, leading to a higher density of covalent bonds in a given unit of area as the test progresses. This would correspond to an increase in the energy required to separate that unit of area (i.e. larger work of adhesion), and therefore changes in the predictions from continuum models as the test progressed.

Further insight is obtained by looking at the atomic-scale interactions in the contact interface. Specifically, a measurement was taken of the areal density of in-contact atoms, using the force criterion. This is loosely analogous to a bond density; however, in the absence of a reactive potential, the concept of a "bond" is not well-defined. For a fixed central region of the contact, this areal density was measured at various points throughout the test, and is shown in in Fig. 2.6(c). The result demonstrates a monotonic increase from the initial value to the value at the highest force. In other words, for a given area of contact, the additional loading has pushed a larger number of atoms into close contact and thus into the deepest part of the interatomic potential. Therefore, this region of contact will require more energy to separate, thus corresponding to a larger work of adhesion in a continuum description. Indeed, high density of in-contact atoms achieved at the maximum force (400 nN) was maintained (within 10%) during unloading until a tensile force of approximately -270 nN is applied. Overall, the 65% increase in "bond" density during loading does not fully explain the measured increase in work of adhesion; however, the qualitative trends are similar. Therefore, the present results are at least consistent with an adhesion hysteresis that arises due to stress-dependent bond formation across the interface. Further simulations with a reactive potential are required to explore the details of the bond formation and breaking under applied force.

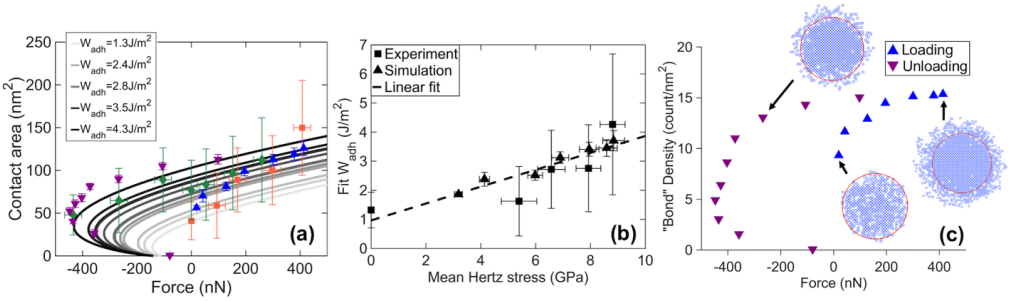

Figure 2.6 The contact area vs force data has been fit (a) using the Maugis-Dugdale model with varying work of adhesion. The effective modulus was set using the best-fit value of 112.1 GPa for unloading (see main text), and the work of adhesion is varied to separately match each individual point in the loading curve. The result of this point-by-point fit (b) shows a monotonically increasing value of work of adhesion with increasing mean Hertz stress. The simulation results were used to compute the areal density of in-contact atoms (c) in the central region of contact (red circle). The initial contact area shows a lower density of "bonds", which increases monotonically throughout loading. Notably, the high final "bond" density is maintained during unloading to large negative forces. Experimental data is provided by Professor Tevis Jacobs' research group in University of Pittsburgh.

2.8 Conclusions

This investigation comprised a comprehensive analysis of the loading and separation of a nanocontact using molecular dynamics simulations. The simulations were matched with a physical realistic experiment regarding materials, geometry, structure, crystal orientation, and applied forces. The Buckingham potential was used to model the interactions across the interface, and to reproduce the pull-off force observed in the *in situ* TEM experiment. First, it was demonstrated that the choice of method for computing contact area can lead to significant variations in measured results. Second, the experimental and simulated measurements for contact area as a function of applied force demonstrated hysteretic behavior, with larger values measured upon unloading as compared to loading. Therefore, they could not be accurately fit using a straightforward application of continuum mechanics via the Maugis-Dugdale model. For contact area, the Maugis-Dugdale model could be fit to the unloading portion of the contact area curve with a reasonable value of effective elastic modulus extracted from the fit; however, the same model over-predicted contact area by an average of 46% during loading. Further, the contact area varied dramatically depending on the measurement technique. Therefore, an alternative method is required to corroborate results. One approach is to use an indirect measurement of contact area, such as conductance. However, as discussed in the next chapter, this approach too has limitations, specifically related to the effect of insulating layers on conductance measurements.

Chapter 3 Conduction of metallic contacts at the nanoscale

3.1 Introduction

Numerous investigations over the last two decades have applied these electrical transport theories to metal nanocontacts. For example, several studies have used these theories to measure the size of the tip/sample contact in conductive AFM [8, 20, 91]. More recently, a combined c-AFM and simulation investigation used the ballistic transport equation to describe electrical transport through a conductive doped ultra-nanocrystalline diamond tip and a graphene sheet [92]. Further, various analytical models have been proposed to describe electrical transport through technologically relevant devices such as microelectromechanical systems (MEMS) switches [93, 94, 103, 95–102]. These models describe microcontacts, which have inherent roughness, as an array of smaller point contacts, each of which is described by the intermediate transport theory. These transport theories are also used in first-principle calculations for modelling electrical resistance for copper interconnects [104]. Finally, recent electrical characterization of metal nanostructures have suggested the applicability of the ballistic theory to describe electrical transport in silver nanowires [105]. These examples represent a small sampling of the broad application of transport theories to metal nanocontacts in a wide range of advanced technologies.

However, some investigations suggest the failure of electrical transport theories to describe transport through nanocontacts, even for noble metals. *In situ* TEM investigation on gold nanocontacts [51] showed lower conductance than expected from an intermediate theory. Other nanoindentation measurements combined with MD simulations of a tungsten/gold contact also showed lower conductance than expected using ballistic theory [106]. These studies suggested that the observed behavior is caused mainly due to significant scattering by the defects at the interface [51, 106]. Furthermore, experimental investigation [107] of single asperity platinum contacts using atomic force microscopy has suggested the formation of an insulating tribopolymer layer after billions of loading and unloading cycles. Additionally, atomistic simulations have suggested a significant decrease in conductance with just a 0.36-nm thick layer of adsorbates [108]. Density functional theory (DFT) simulations [109] have indicated that platinum contacts can form carbonaceous surface layers under the action of mechanical stress and voltage. Significant work has been conducted to understand the electrical transport on single asperity contacts, however there is still a lack of quantitative understanding of contact size and current flow between nanoscale bodies in contact.

The objective of the present investigation is to simultaneously measure the contact size, current flow, and applied forces on single asperity platinum nanocontacts using MD simulations that mimicked the *in situ* TEM experiment, and thus to provide a model that would best describe current flow across this contact. All the experimental data in this chapter are provided by Professor Tevis Jacobs' research group in University of Pittsburgh.

3.2 Methods

Molecular dynamics simulations were performed on matching model nanocontacts. The models were created to match the experimental probes in their materials, geometry, structure, crystallographic orientation, and applied and adhesive forces. Specifically, the high-resolution TEM images were traced [110] to obtain the geometry and crystal orientation of the platinum probes (Fig. 3.1a). A 3D atomistic model of the platinum probe and substrate was created using the TEM-determined crystal orientation and geometry (figures 3.1b,c). The detailed simulation procedure can be found in Ref. [111]. The embedded-atom method (EAM) potential was applied to simulate the interaction of atoms within the probe and the substrate [112]. A Lennard-Jones potential was used to model interactions between the probe and substrate to reproduce the interfacial interaction strength in experiments, which could be affected by factors that are not explicitly captured in the EAM potential (e.g., adsorbates, surface defects, and surface oxidation). The interaction strength ε of the Lennard-Jones potential was tuned so that the simulation and experiment had the same pull-off force. The zero-potential-energy distance σ was chosen based on Ref. [113].

The simulation was used to determine both the number of atoms in contact as a function of load, as well as the overall area of contact between the two bodies. The contact atoms were identified using a force criterion where an atom in the probe was considered to be "in contact" if the time-averaged interaction force between it and the substrate was repulsive [48, 49]. After determining the contact atoms, the contact diameter ($2a$) was measured as the length of the contact as viewed from the side, in direct analogy with the TEM data. In the latter case, to rule out the effect of the viewing orientation, results were averaged from six different viewing directions (corresponding to 0° along the y axis, as well as 30°, 60°, 90° along the x axis, 120°, and 150°). Methods for calculating contact area from an atomistic simulation are discussed in detail in Ref. [114].

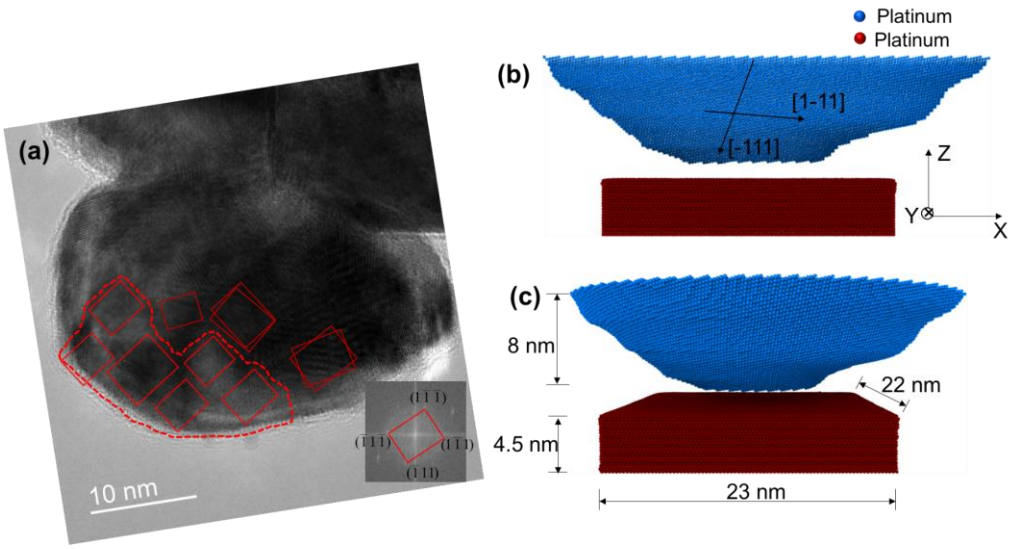

Figure 3.1 TEM (a) images of the experimental setup consisting of an in situ contact test inside of a transmission electron microscope. A flat Pt indenter is opposite a Pt AFM chip, such that it can be brought into contact with the nanoscale tip. The red rectangular box represents the crystallographic directions of the Pt. Close up, side (b) and perspective (c) view of the atomistic model of the model Pt AFM tip apex coming into contact with an ideally flat Pt surface. The tip and substrate are both Pt, but shown here in different colors for clarity. Experimental data is provided by Professor Tevis Jacobs' research group in University of Pittsburgh.

3.3 Results and discussion

3.3.1 Adhesion tests: Comparing measurements of contact size and current flow

Figure 3.2 shows a comparison of the directly-measured contact radius obtained from TEM and atomistic simulations against the computed contact radius obtained from applying electrical transport theories to the measured current flow. The five individual tests showed consistent results within the uncertainty of the measurements (figures 3a,b) and the simulation-determined contact radius matched well with the contact radius obtained from TEM videos. Here, the contact size was computed from experimentally-measured conductance using both limits (Sharvin and Maxwell), with known property of bulk conductivity $\sigma_{bulk} = 94.3 \times 10^{-3}$ $(\mu\Omega\ \mathrm{cm})^{-1}$ of platinum [90, 115–117] and calculated mean free path length $l_f = 7$ nm using free electron model [116]. The results show that the contact radius calculated from the current flow using ballistic and diffusive electrical transport theories is, on average, 93% smaller than the direct measurements. This suggests that these transport theories do not accurately describe the present contact. The physical origin of this discrepancy is discussed in the next section.

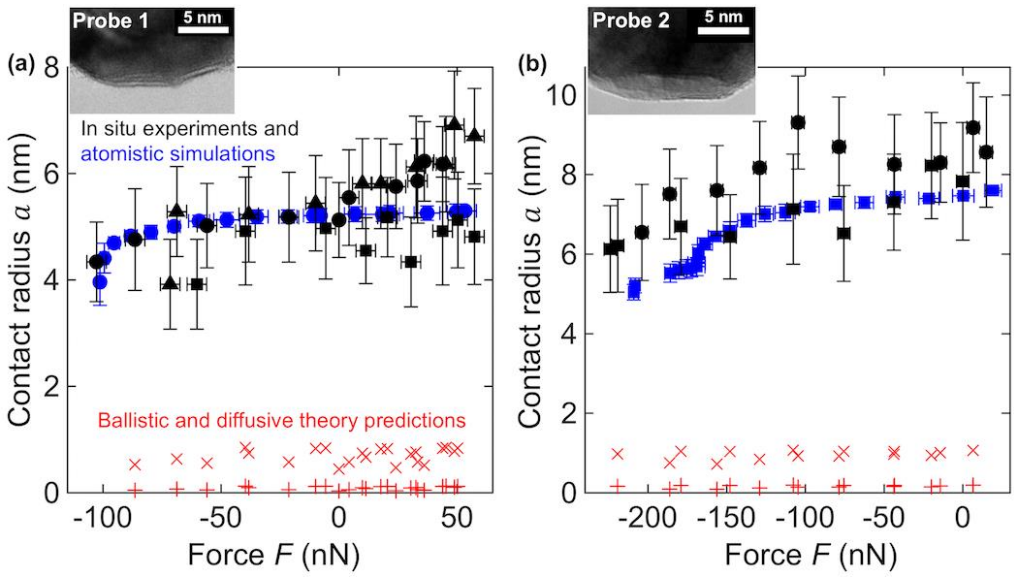

Figure 3.2 The directly measured contact radius varies significantly from the value computed from electrical measurements. The contact radius from in situ experiments (black symbols) and atomistic simulations (blue symbols) is shown as a function of applied force. Multiple repeated measurements showed consistent results for two different platinum nanoprobes (shown separately in panels (a) and (b)). The contact radii computed from the electrical measurements, using the limiting cases of diffusive (crosses) and ballistic (plus symbols) transport, were lower than the direct measurements by at least 93%. Experimental data is provided by Professor Tevis Jacobs' research group in University of Pittsburgh.

3.3.2 Investigating the physical origin of the low contact conductance

To explore the physical origin of the lower-than-expected conductance, we considered three possible hypotheses. (1) The current flow is reduced because of significant inelastic scattering of electrons at defects in the near-surface region. (2) The true atomic contact area is much smaller than the apparent contact area due to, for example, atomic-scale corrugation and surface roughness, thus significantly reducing current flow. (3) The presence of thin insulating surface species, such as oxygen or adventitious carbon, significantly reduces the metal-metal contact or eliminates it altogether, requiring electron tunneling. These are considered individually in the following paragraphs.

The basis for the defect-scattering hypothesis (Hypothesis 1) is prior work, including that of Mayadas and Shatzkes [118], which demonstrates significant scattering from defects in confined systems. While defect scattering is negligible in bulk contacts, it is a significant factor in nanograined metals which have a large density of crystal defects [119]. Prior work by the present authors has shown that the defect density in the near-surface region is very large, even at ultra-low (adhesion-only) loads [111]. The defect-scattering hypothesis leads to the specific prediction that the degree of electron scattering will be inversely

proportional to the defect spacing in the material [118]. To test this prediction, the scattering factor was computed in the present work and compared to the defect density in the material (which is inversely proportional to the defect spacing). Instead of the ratio of ρ/ρ_{bulk} used by Mayadas and Shtazkes for large 2D films, we computed the scattering factor as the ratio of conductance predicted using the intermediate theory (G_I, computed using Eq. 2 with the TEM-determined contact size) divided by the measured conductance G from the experiment. As shown in figure 4a, while there is significant reversible plasticity in the material and the length of dislocations increases significantly, the measured scattering factor exhibits no consistent trend with force. Thus, the predictions of the Mayadas and Shtazkes model are not supported by the data, which suggests that scattering from defects is not the primary cause of low conductance in these contacts.

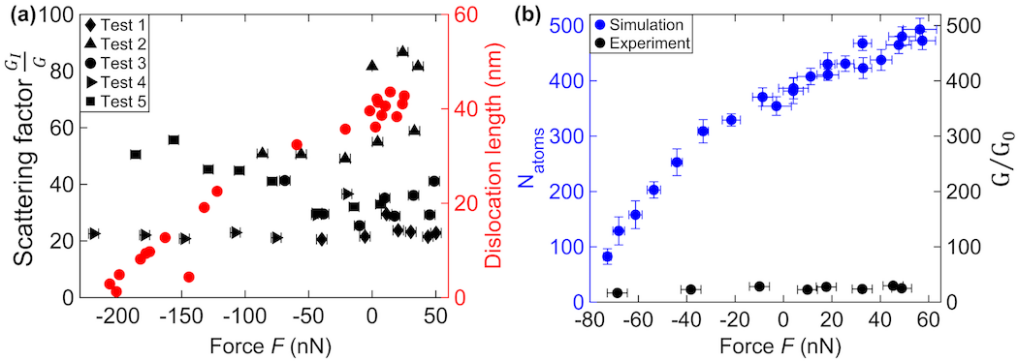

Figure 3.3 To evaluate the effect of electron scattering from defects, a scattering factor (a) was computed (see main text) and compared to the length of dislocations in the tip material. No correlation between these was observed, with scattering factor approximately constant with force for most tests and dislocation length increasing monotonically. Thus, the defect-scattering hypothesis is not supported. The dislocation vs. force data is taken from simulations reported in prior work [111]. To evaluate the possibility of roughness-induced incomplete contact, the number of atoms in contact (b) was determined from the atomistic simulations and compared to the ratio G/G_0, which would reflect the number of contact atoms in the case of ballistic transport across a number of very small contacts. These two curve exhibits very different magnitudes and trends with force, implying that this is not the cause of the low contact conductance. Experimental data is provided by Professor Tevis Jacobs' research group in University of Pittsburgh.

The hypothesis of patchy atomic contact (Hypothesis 2) is based on prior experimental investigation of the electrical and thermal transport across the nanoscale interfaces [27, 120] as well as atomistic simulations of nanoscale probes [27, 42, 48, 63, 120, 121], which have suggested that the true atomic contact that contributes to transport may be much smaller than the overall contact area. This is commonly attributed to surface roughness, even down to atomic-scale corrugation of the surface. Roughness or corrugation cause the contact to behave as a collection of atomic-scale point contacts, rather than a single nanoscale junction, resulting in significantly reduced transport. In the present testing, the

idea of patchy contact can be tested by directly computing the number of contact atoms from the molecular dynamics simulations and comparing to the number of contact atoms calculated from the conductance. The latter quantity is computed by dividing the total measured conductance by the conductance quantum G_0 (12.9 $k\Omega)^{-1}$ [65, 122–126]. If the nanocontact is behaving as a small number of atomic junctions, then G/G_0 should be approximately equal to the number of atoms in contact. As shown in figure 3.3b, the number of contact atoms from the simulation is far greater (between 8 and 19 times greater) than the computed number of contact atoms determined from the electrical conductance. Further, it can be observed from figure 3.3b that at the maximum force of 57 nN, the number of atoms in contact in the experiment are 25 in comparison to 500 from simulations. This implies that roughness and patchy contact result in a 95% reduction in contact area. This seems extremely unlikely as it would require the remaining 5% of the contact atoms to carry twenty times more load per atom than for full contact. The contact stress was already large (9 GPa at maximum force, as calculated using contact mechanics models and assuming full contact), and a 20-fold increase above this would almost certainly lead to flattening of any local protrusions. Such flattening would result in near-complete contact. It should also be noted that any such roughness would be explicitly rubbed off in the sliding tests; yet these tests showed no significant increase in conductance. These findings suggest that the failure of ballistic transport equations cannot be explained by surface roughness and atomic corrugation.

Finally, in the surface-species hypothesis (Hypothesis 3), the low conductance arises because of insulating species that are present on the surface, likely either oxygen or adventitious carbon from exposure to air before testing. In this case, tunneling theory [127] is expected to predict the electrical transport better than ballistic or intermediate models. For an insulating layer between two similar metals, at very low voltages, Simmons *et. al* [127] provided an expression for the current density J (in units of A/m^2) as a function of applied voltage V in volts (V) as

$$\mathrm{J} = 3.16 \times 10^{14} \sqrt{\phi} \left(\frac{V}{\Delta z}\right) \exp\left[-1.025 \Delta z \sqrt{\phi}\right] \tag{3.1}$$

where ϕ is mean barrier height (eV), Δz is barrier width (Å) which can be assumed to be thickness of the insulating layer [127]. For fixed values of ϕ and Δz, the current density is linearly proportional to applied voltage, similar to the behavior of Ohmic contact [127]. Hence, Eq. 3.1 can be written in terms of conductance, contact area $A_{electrical}$, and tunnel resistivity $\sigma_T (= V/J)$ as follows

$$G = \frac{A_{electrical}}{\sigma_T} \tag{3.2}$$

where G is in Ω^{-1}, $A_{electrical}$ is in cm^2, and σ_T is in Ω cm^2.

The tunneling model described by Eq. 3.2 is fit to the experimental data (figure 3.4a) with tunnel resistivity as the free parameter. The extracted best fit for σ_T is 6.7×10^{-10} Ω cm^2. The order of magnitude of the best-fit tunnel resistivity is reasonable for an insulating material having thickness less than 2 nm at very low voltages [127]. The tunnel resistivity σ_T is a function of mean barrier width and potential barrier of the insulating material.

Specifically, using the best-fit tunnel resistivity and the measured thickness of the layer, the potential barrier ϕ can be determined. High-resolution images of the probes before and after contact were used to attempt to determine the thickness Δz of the hypothesized insulating layer. As shown in figure 3.4b, the platinum appears to persist all the way to the surface, with no clear surface layer observed. Therefore, we used the resolution of the TEM (0.23 nm) as an upper-bound estimate of the thickness of the surface layer, which is consistent with earlier work using aberration-corrected environmental TEM to oxidize and reduce a platinum surface [128]. Using the best-fit tunnel resistivity (6.7×10^{-10} Ω cm^2) with a layer thickness of 0.23 nm, the barrier height computed using Eq. 3.1 is 0.8 eV (figure 3.4c). The electrical contact area predicted using Eq. 3.2 is consistent with direct measurements of experiments and simulations (figure 3.4d).

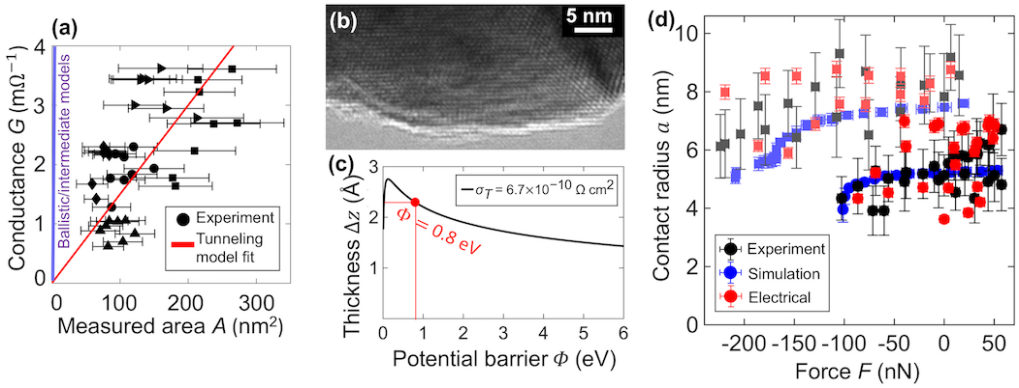

Figure 3.4 The conductance across the platinum nanocontact (a) is proportional to the experimentally observed contact area, within experimental uncertainty, but is not consistent with ballistic and intermediate theories. Under the assumption of electron tunneling, the proportionality constant yields a measure of the tunnel resistivity. Since surface species cannot be observed in high-resolution TEM (b), the imaging resolution (0.23 nm) is taken as an upper-bound of the insulating film thickness. These data can be combined with tunneling theory (c) to measure a potential barrier for the surface layer of ϕ = 0.8 eV. Using tunneling-mediated transport with the best-fit parameters, the electrical measurements can be used to extract a contact size (shown in d) that is consistent with experiments and simulations. Experimental data is provided by Professor Tevis Jacobs' research group in University of Pittsburgh.

3.3.3 The implications of the present findings

While it was already well known that small amounts of oxide or contamination can affect contact conductance, this investigation demonstrates the significant and persistent role that surface layers play in nanoscale contacts composed of platinum. Even when tested in vacuum, and with the contact subjected to sliding wear, the conductance remains significantly lower than what is predicted by electrical transport theory. The persistence of this surface layer may arise due to tribochemical processes that occur on platinum contacts [109]. It has been shown using DFT that the polymerization reactions could take place with a threshold stress of 24 GPa on a flat platinum surface and this threshold stress can be even

lower due to shear stresses as well as surface steps and vacancies [109]. In the present investigation, the maximum contact stress reached during loading is more than 9 GPa. (This is the value computed using contact mechanics models applied to the overall tip shape [15], but local asperities will concentrate the stress higher than this value). Also, the simulations provide evidence for surface steps which can be observed on the model AFM probe (figures 3.1b,c). Hence, these tribochemical processes could explain the presence and robustness of the insulating monolayer.

The present findings of low contact conductance shed some light on the widely observed [91, 107, 120, 129] phenomena of higher-than-expected contact resistance in conductive AFM. For instance, Celano and co-workers [120] introduced a precise calibration procedure to determine the electrical contact area of an AFM probe. Current-voltage sweeps were performed on a silicon oxide substrate of precisely 1.5 nm thickness; then, using tunneling theory to describe the conductance through the oxide, the size of the current collector (i.e., the contact) could be directly determined. From measured current flow through a Pt/Ir probe, a contact radius of just 0.69 nm was computed at a load of 78 nN and 0.97 nm at 157 nN. The authors commented on this being far smaller than the expected size from contact mechanics with an assumed probe radius of 30 nm. The authors do not suggest an explanation for this ultra-small size, except potentially microroughness (yet TEM images [107] of similar probes from the same manufacturer do not demonstrate such extreme roughness). The present results rule out this type of roughness as the origin of the low current, as well as defects in the near-surface material, and instead suggest an explanation for the ultra-small measured contact size. The nanoscale metallic probe itself is suggested to have lower-than-expected conductance, due to surface species which are not accounted for in Celano's investigation. If we apply an empirical correction (Eq. 3.2) to this calculation, where the contact conductance is 95% smaller than predicted by ballistic transport theory, then the computed contact areas rise from 1.5 nm^2 to a value of 30 nm^2, which is consistent with the authors' prediction of 28 nm^2 for a 78 nN load.

3.4 Conclusions

In summary, atomistic simulations were performed on similar platinum nanoprobes with matched geometry, crystallographic orientation, loading direction, and applied and adhesive loads. The application of electrical transport theories to the measured conductance yielded measurements of contact size that were 93% smaller than the experimental and simulation values. Two possible explanations for the lower-than-expected contact conductance were ruled out: electron scattering from crystal defects; and a roughness-induced reduction in contact area. Instead, the physical mechanism for this deviation from electrical transport theories was found to be the presence of insulating surface species. The observed reduction in contact conductance was consistent despite loading and sliding of the probe, and was maintained even despite significant variations in probe shape. Tunneling theory was empirically fit to the data, based on approximately monolayer (roughly 0.23 nm) coverage of insulating species with a measured potential barrier of 0.8 eV. It is suggested that this description, tunneling theory with these parameters, provides a more robust method than classical electrical transport theory for the calculation

of contact area for single asperity platinum contacts from the current-voltage data in AFM, and for the prediction of current in platinum nanodevices.

Chapter 4 Effect of native oxides on contact area measured through conductance

4.1 Introduction

Conductive atomic force microscopy (c-AFM) has enabled the indirect measurement of contact area through the electrical contact conductance. In c-AFM, a bias voltage V is applied between the tip and substrate, the resultant current I is measured, and the electrical conductance G is determined from slope of the I-V curve. Then, under the assumption that contact radius a is smaller than the mean free path of an electron l_f, it is common to relate conductance and contact area using the Sharvin equation for ballistic transport:

$$G_s = 3A_S/4\rho l_f \tag{4.1}$$

where ρ is resistivity and A_S is contact area. The proportionality of conductance and contact area has been shown to be accurate for nanometer scale contacts [9, 130, 131], and even for metallic junctions thinned down to single-atom width [26, 132]. However, the Sharvin equation does not account for the presence of insulating layers on the contacting surfaces. Such insulating layers, including oxides, adsorbates, or contaminants, are common on surfaces in real-world applications and under most experimental conditions [133, 134]. The presence of insulating layers can prevent the formation of metallic contact, and prior work by the present authors suggests that, in such cases, electronic transport theories can overpredict current flow across a platinum nanocontact by a factor of 20 [135]. This overprediction is due to the fact that, with an insulating film, conduction only occurs by tunneling across the interface. In this case, the relationship between conductance and contact area A_T is described by tunneling theory [135, 136]:

$$G_T = \left(3.16 \times 10^{14}\sqrt{\phi}\frac{1}{t}\exp\left(-1.025t\sqrt{\phi}\right)\right)A_T \tag{4.2}$$

where ϕ is the mean barrier height and t is the oxide thickness. This tunneling model has been used calculate contact area from c-AFM measurements with an oxide-containing conductive platinum tip [135, 137].

Therefore, previous research suggests that ballistic transport theories can be used to calculate contact area from conductance if no insulating layer is present and tunneling theories apply for a thick insulating layer. However, many real contacts may exist between these limiting cases. For example, Pt is relevant for many applications that rely on nanoscale contacts [81, 83, 138] and Pt surfaces may have a native oxide layer that is less than 0.5 nm thick [135, 139]. The accuracy of ballistic transport or tunneling theories for calculating contact area in these cases is unknown because area and conduction cannot be measured independently. Furthermore, a common approach in experimental studies is to simply use c-AFM with the Sharvin equation, regardless of the possible presence of thin insulating layers [130, 140, 141].

Atomistic simulations can provide some insight into the effect of insulating layers because they explicitly model the size and morphology of the contact. Density functional theory or *ab initio* molecular dynamics enable the direct calculation of conduction [52–56], but are

limited to very small size scales and so cannot capture the deformation at technologically relevant size scales. Alternatively, classical MD simulations can model nanoscale contacts accurately [58, 135], but do not include electrons and so cannot directly calculate conduction. There have been extensions of classical MD developed that enable calculation of conduction [41, 57], but the approach does not differentiate between atom types and so cannot be used to investigate the effect of insulating layers. Finally, a recent study by Yang, *et al.* [58] used classical MD simulations to understand the effect of small amounts of adsorbates on conduction in Pt nanoasperities for nanoelectromechanical switches. The authors showed that adsorbates can partially or completely block metal-metal contact, and described a balance where some adsorbates are advantageous for minimizing plastic deformation, but too many adsorbates will block the current flow. However, this study considered current flow through direct metal-metal contact and did not attempt to include contributions due to tunneling, which may play a significant role in the case where one or more of the metals has at least a full monolayer of oxide coverage.

In the present study, we used MD simulations to model the nanoscale contact between a platinum tip with an oxide and a pristine platinum substrate, where conductance was approximated using an empirical model that included both direct metallic and tunneling conduction. The goal was to evaluate the accuracy of contact area measurements obtained using conventional experimental c-AFM techniques with ballistic transport theories when a thin oxide layer is present. The approach consisted of five steps: (1) Identify channels of platinum atoms across the interface; (2) approximate total conductance based on an empirical model relating conductance to atom distance in the channels; (3) calculate contact area from the conductance using ballistic transport and tunneling theories; (4) calculate the *true* contact area using positions of atoms in the contact; and (5) determine the difference between contact area calculated from conductance and that from atom positions as a function of oxide thickness. The contact area calculated from conductance is comparable to the approach used in a typical c-AFM experiment, so the difference between this value and the area obtained from atomic positions reflects the error that might be expected in an experiment.

4.2 Methods

Figure 4.1(a) shows a snapshot of a model oxide-coated platinum tip and atomically flat platinum surface. The Pt tip was parabolic with a radius of 2 nm and a height of 5 nm. The tip radius and height were chosen to be big enough to minimize the effects of boundaries on the contact stress distribution [142]. The crystalline region of the tip had a crystallographic orientation of [1 -42 31] in the z-direction. This orientation was randomly chosen, but was selected to ensure a rounded tip apex could be achieved for this small tip size. The dimensions of the flat Pt substrate were $9.0 \times 8.8 \times 3.0$ nm^3 in x-, y-, and z-directions, respectively, with a crystallographic orientation of [1 1 1] in the z-direction. Periodic boundary conditions were applied along the x- and y-directions and the boundary was fixed in the z-direction.

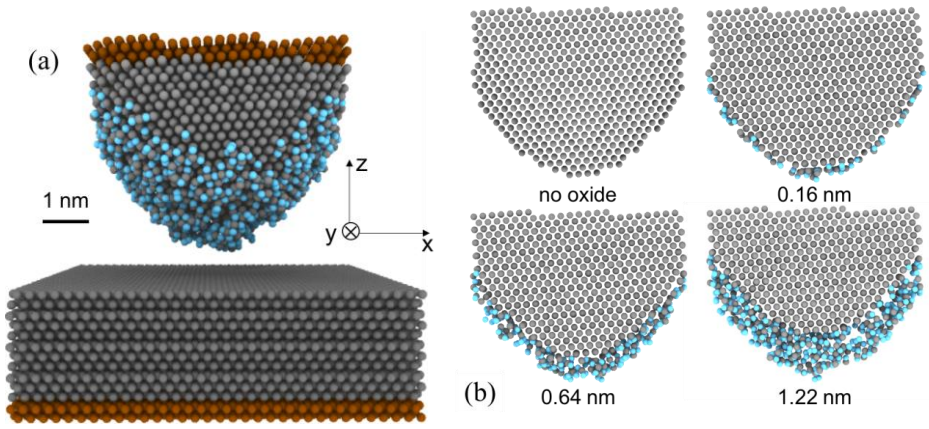

Figure 4.1 (a) Snapshot of the model of an oxide-coated Pt tip and a flat Pt counter-surface; (b) Cross-sections of the Pt tips with varying oxide thickness: 0 nm (no oxide), 0.16 nm (approximately one monolayer), 0.64 nm, and 1.22 nm. The outermost radius of all model tips is 2 nm. The grey color represents platinum atoms, the blue color represents oxygen atoms and the brown color represents rigid platinum atoms.

The topmost 0.5 nm of the tip and the bottommost 0.5 nm of the substrate were treated as rigid bodies. A Nosé-Hoover thermostat was applied to the 2-nm region adjacent to the rigid layers in both tip and substrate to maintain the temperature of the system at 300 K. The remainder of the tip and the substrate were integrated using the NVE (constant number of atoms, volume, and energy) ensemble, which ensured interactions of the atoms between the tip and the substrate without a significant effect of the thermostat [70]. All interatomic interactions were modeled using the ReaxFF potential [143] with a time step of 0.25 fs. This potential was previously shown to predict the bulk properties of Pt, as well as oxygen adsorption and oxide formation on Pt surfaces, in reasonable agreement with both density functional theory calculations and experiment observations [143, 144]. Simulations were carried out using the large-scale atomic/molecular massively parallel simulator (LAMMPS) [145].

Seven model tips were created by combining a crystalline Pt core with amorphous Pt oxide shells of varying thickness. First, a periodic box containing amorphous platinum dioxide was created by heating α-PtO_2 to 2000 K and then quenching to room temperature. α-PtO_2 was used since the surface oxide for platinum usually has a Pt-to-O ratio of 1:2 [139, 146]. Then, a thin shell of oxide was cut from the box where the inner radius of the shell was the same as the outer radius of the crystalline Pt core. Simulations were run at 500 K until the potential energy reached steady state, which required an average of 7 ps. After the oxidized Pt tips equilibrated, the thickness of the oxide layer t was re-characterized by calculating the average distance between the crystalline profile and the oxide profile at 40 positions on a cross-section of the tip. Seven Pt tips were created with varying oxide thickness: 0 nm (no oxide), 0.16 nm (approximately one monolayer), 0.40 nm, 0.64 nm, 1.00 nm, 1.15 nm, and 1.22 nm; four of these are shown in Fig. 4.1(b).

Each Pt tip was initially placed such that the center of the bottommost atom of the tip was 1 nm above the center of the topmost atom of the substrate. This distance is larger than the cutoff distance of the potential which ensured that there was no interaction between the tip and the surface at the start of the simulation. The tip was then brought into contact with the surface at a speed of 10 m/s. During this process, the penetration of the tip into the substrate δ was calculated as the instantaneous distance between the center of atoms in the rigid layers subtracted from the sum of the initial heights of the tip and substrate. This calculation of penetration depth is consistent with the definition used in typical contact mechanics models [147], where zero corresponds to the point at which the tip and substrate would first come into contact if they were rigid bodies. At various times, the tip movement was stopped and the model was relaxed for 50 ps to ensure stable energy and force.

4.3 Results and discussion

To approximate the conductance of the contact between the Pt tip and substrate, we assumed conduction occurred through "channels" of Pt atoms that spanned from the substrate to the crystalline region of the tip. Figure 4.2(a) shows a representative conduction channel for the model with 1.15 nm oxide. To identify a conduction channel for a given substrate atom (atom 1 in Fig. 4.2(a)), we first found the nearest Pt atom (atom 2) in the tip. Then we searched for the next Pt atom (atom 3) which was closest to atom 2 in the tip. This process continued until the next Pt atom (atom 7) was within the crystalline region of the tip. After identifying a metallic chain, we searched for O atoms between Pt atoms in each chain based on the following criteria: the vertical position of the O atom is between those of two Pt atoms, and the distance between the O atom and each Pt atom is smaller than the distance between the two Pt atoms. Figure 4.2(a) shows an O atom identified between Pt atom 5 and Pt atom 6. This process was repeated for every atom on the surface of the substrate. Once all possible channels were identified, we approximated conduction as described below.

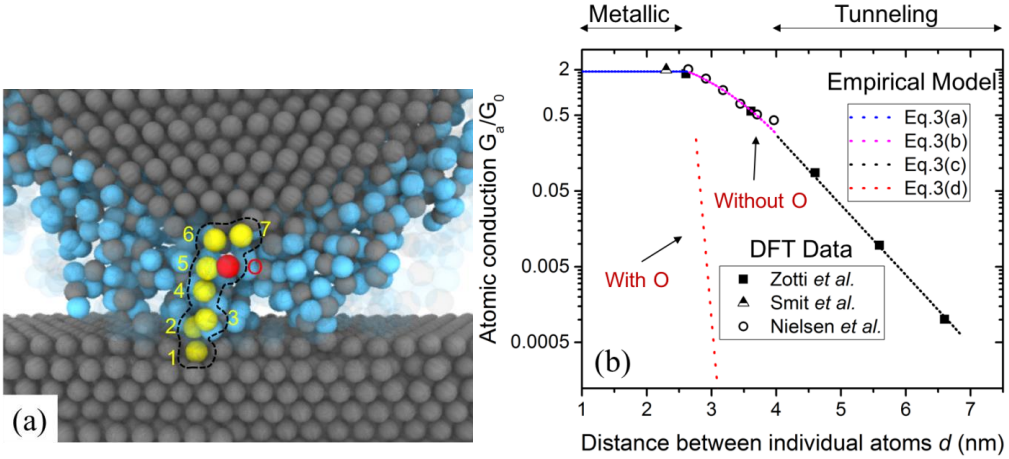

Figure 4.2 (a) A representative conduction channel (Pt in yellow) was identified with an oxygen atom (red) present for the contact model with 1.15 nm oxide. (b) Conductance was plotted as a function of distance d between individual atoms. The original data were taken from Ref. [56] (solid squares), Ref. [148] (half solid

triangles), and Ref. [53] (hollow circles). Conductance is approximated using an empirical model (dotted lines) that includes both metallic and tunneling conduction, where blue, pink, black lines are the fitting empirical model without oxygen present, red line represents the empirical model with oxygen.

Conduction along an atomic channel can occur through two mechanisms, direct metallic contact conduction or tunneling, depending on the distance between atoms. Direct metallic conduction occurs when atoms are close enough for electron transport to occur by ballistic or diffusive mechanisms [26]. The direct metallic conductance of a single Pt atom chain has been found to be 1.5~2.5 G_0 [53, 122, 148–150], where G_0 is the quantum conductance ($G_0 = 2e^2/h$). As the distance between atoms increases, the conduction shifts from metallic conduction to tunneling conduction [136]. Previous density functional theory (DFT) calculations have shown that conduction between atoms decays exponentially as their distance increases [53–56].

Here, we used DFT data from Refs. [53, 56, 148] to develop an empirical model (Eq. 4.3) for atom-atom conductance G_a as a function of atom center distance d that captures both the constant conductance of direct metallic conduction and the distance-dependent conductance of tunneling conduction. For atom-atom distances less than 0.27 nm, the conductance was taken to be 1.89 G_0, the average of values reported from previous DFT calculations for direct metallic conductance [53, 56, 148]. For distances larger than 0.27 nm, two exponential decay functions were used, chosen to fit the available DFT data [53, 56], where the decay rate was larger for distances greater than 0.4 nm when conduction occurs via pure tunneling. Further, studies have shown that the conduction in silver and copper atom chains decreases if oxygen is present [151, 152]. This effect has also been shown for platinum with a hydrogen molecule or carbon and oxide atoms embedded in the chain [150, 153, 154]. Unfortunately, no previous data is available for platinum chains with oxygen. Therefore, we developed an approximate function based on the expectations that (i) the conductance will decay more quickly with oxygen than without, and (ii) for the thickest oxide (1.22 nm) the total conductance should be consistent with the prediction of classical tunneling theory (Eq. 4.2). The complete set of equations used to estimate conductance based on atom distance is the following:

$$\frac{G_a}{G_0} = \begin{cases} 1.89, & \text{for } d \le 0.27 \text{ nm} \quad (4.3a) \\ e^{\left(1.46d - 0.43d^2 - 0.24\right)}, & \text{for } 0.27 < d \le 0.4 \text{ nm and without O} \quad (4.3b) \\ e^{\left(-2.13d + 7.21\right)}, & \text{for } d > 0.4 \text{ nm and without O} \quad (4.3c) \\ e^{\left(-23.00d + 61.47\right)}, & \text{for } d > 0.27 \text{ nm and with O} \quad (4.3d) \end{cases}$$

The available DFT data and empirical approximations are shown in Fig. 4.2(b). We note that these equations are approximations based on previous DFT data and limiting behavior predicted by classical tunneling theory, but are not expected to provide exact quantitative predictions of conductance.

Eq. 4.3 was used to calculate the conductance for all atom-atom pairs and the conductance for each channel $G_{channel}$ was taken as the minimum conductance for atom-atom pairs G_a in that channel, based on the assumption that ballistic transport though an atomic-sized ballistic contact is independent of length[26]. Then, the total conduction for the system G was calculated as the sum of the conductance of all channels acting as resistors in parallel, i.e. $G=G_{channel,1}+G_{channel,2}+\ldots+G_{channel,N}$. The total conductance was calculated using this approach for all model tips as they were brought into contact with the substrate.

Figure 4.3 shows the conductance as a function of time for six different oxide thickness models at a penetration depth of $\delta = 0.06$ nm. At 0 ns, the tip started moving toward the substrate. Then, at 0.073 ns, the downward motion was stopped and the tip was held in place until the system equilibrated. In all cases, the conductance increased during loading and then fluctuated about a constant value during equilibration. Tips with thicker oxide layers exhibited a slower increase in conductance with time and a smaller steady state value.

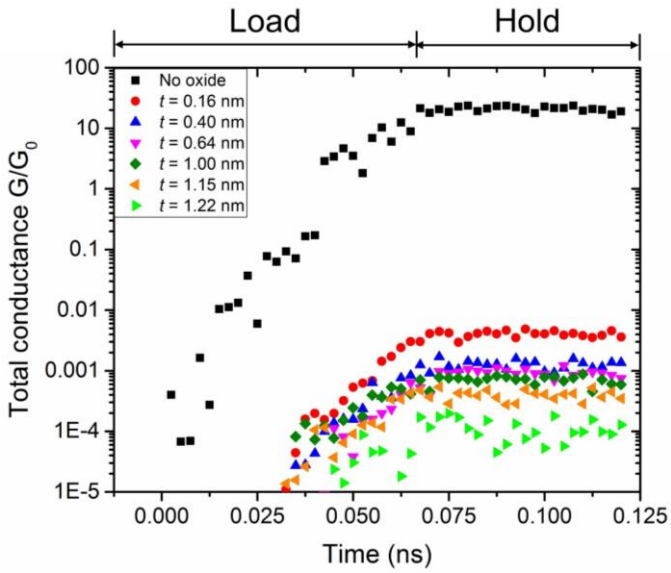

Figure 4.3 The total conductance as a function of time calculated for six different oxide thickness. The tips were brought to the same vertical position (δ = 0.06 nm) and held at that position to allow equilibration.

Figure 4.4(a) shows the conductance as a function of oxide thickness at three penetration depths: δ = 0.06 nm, 0.14 nm, and 0.19 nm, which correspond to average normal loads of -3 nN, 28 nN, and 37 nN, respectively, for the no-oxide tip. The error bars on the conductance reflect the standard deviation of the data during the relaxation period. The position and shape of the tip relative to the substrate at each depth are illustrated in Fig. 4.4(b). In general, the conductance is larger as the tip moves further into the substrate. This is due to both an increase in contact size and a decrease in the distance between atoms in the conduction channels. Also, at all depths, the conductance decays rapidly with

increasing oxide thickness, consistent with observations from experimental studies of insulating films between metal-metal junctions [18, 40, 41].

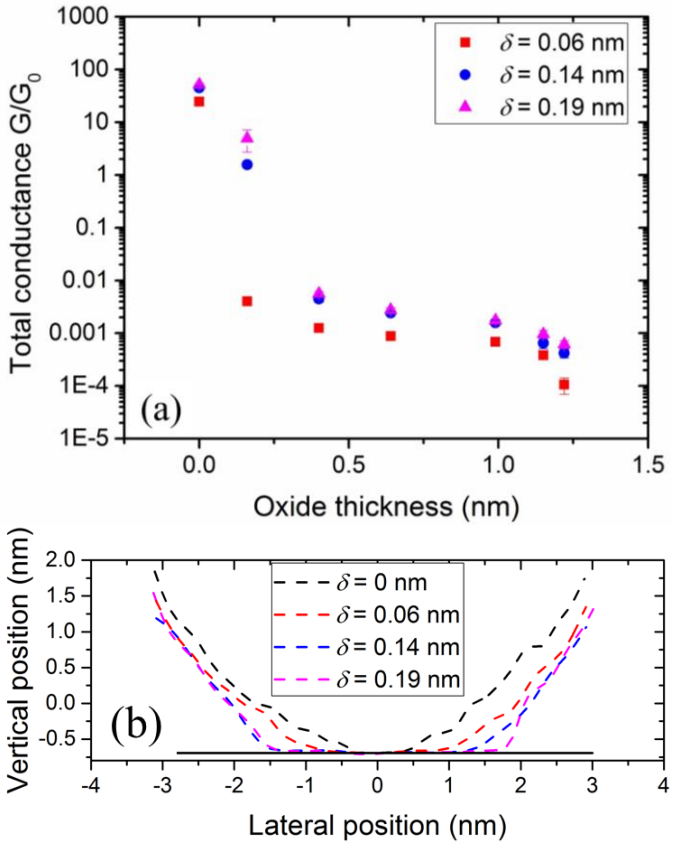

Figure 4.4 (a) The conductance as a function of oxide thickness for three different penetration depths (δ = 0.06, 0.14, 0.19 nm). The error bars represent the standard deviation during the relaxation period. (b) Profiles of the tip at different distances. The dashed lines are the profiles of the tip and the black solid line is the original position of the substrate. These profiles are from the tip without an oxide, but are representative of the other cases.

To mimic a typical c-AFM experiment, the conductance (determined as described above) was used to calculate a measured contact area assuming both ballistic transport and tunneling theory. First, the Sharvin equation (Eq. 4.1) was used to calculate measured contact area A_s, where the resistivity (ρ = 10.6 $\mu\Omega$ cm) and mean free path (l_f = 7 nm) were the values for bulk Pt [135]. Second, the tunneling theory (Eq. 4.2) was used to calculate measured contact area A_T, where the mean barrier height was ϕ = 0.31 eV (reported previously for contact between an oxidized Pt tip and a Pt surface [158]) and the oxide thickness t was measured directly from the simulations. We also calculated a true contact area A_{Atom} directly from the positions of centers of atoms. Specifically, the true contact area was the average of the number of atoms in contact times the approximate area of an atom[47, 48, 50]. Contact atoms were identified as tip atoms within 0.28 nm, the first peak

distance of the radial distribution function of crystalline Pt, of an atom in the substrate, and atom area was approximated as the area of a circle with radius 0.28 nm[47].

The ratio between the contact areas calculated from conductance (A_s or A_T) and the *true* contact area obtained from the atom positions (A_{Atom}) is shown in Fig. 4.5. If there is no oxide, the Sharvin prediction is consistent with that calculated from atom positions. However, as oxide thickness increases, the accuracy of the Sharvin equation decreases, as indicated by the decrease of A_s/A_{atom} from 1 to 0. By contrast, tunneling theory is accurate for the thickest oxides, but underestimates the contact area for thin films, i.e. A_T/A_{atom} increases from 0 to 1 with increasing oxide thickness. Importantly, for oxides between 0.2 and 1.0 nm thick, neither theory appears to be able to capture the actual size of the contact. This thickness range is highly relevant to the studies of c-AFM [135] and MEMS/NEMS devices [159–161].

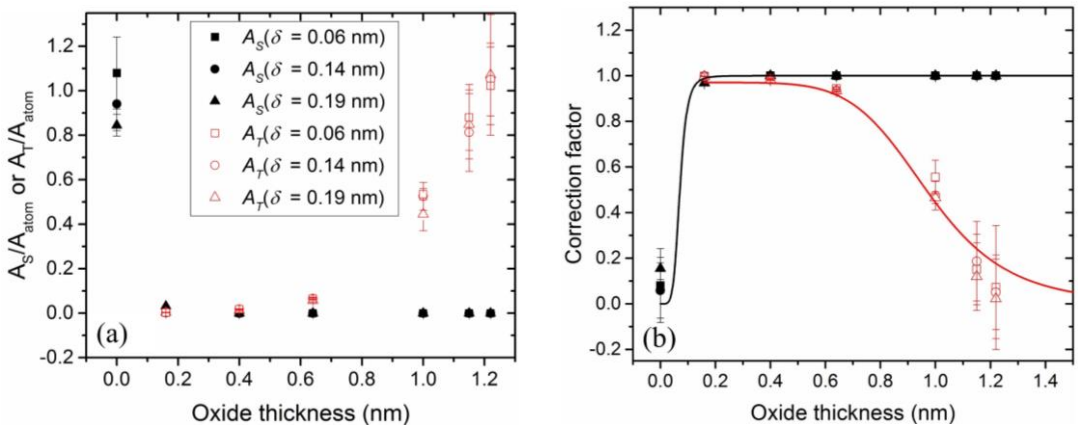

Figure 4.5 (a) The ratio of contact area calculated from conductance using the Sharvin equation (A_S, black solid symbols) and tunneling theory (A_T, red hollow symbols) to the area calculated from atom positions at different tip-substrate depths (indicated by marker shape). (b) Correction factor for measurement of contact area as a function of oxide thickness, where the symbols have the same meaning as in (a) and the lines correspond to Eqs. 4(a) for ballistic transport (black line) and 4(b) for tunneling (red line).

To quantify the effect of an oxide on the contact area calculation, we calculated the normalized difference between the true contact area calculated from atom positions and area calculated from conduction as $c_{S/T} = 1 - \frac{A_{S/T}}{A_{atom}}$. This term represents a correction factor that could be used to calculate true area from a conduction measurement. Figure 4.5(b) shows the correction factor as a function of oxide thickness. We fitted empirical functions to the contact area data obtained using the Sharvin (c_S) and tunneling (c_T) theories:

$$c_S = 1 - \frac{1}{1 + (\frac{2.10t}{t_0})^{5.42}} \tag{4.4a}$$

$$c_T = \frac{1}{1 + (\frac{0.15t}{t_0})^{5.66}} \tag{4.4b}$$

where $t_0 = 0.15\,nm$ is the thickness of a monolayer oxide. The coefficient of determination R^2 is 0.99 for c_S and 0.96 for c_T. For an infinitely thick oxide, these equations predict 100% difference for the Sharvin equation and 0% difference for tunneling theory; in the absence of an oxide, the reverse is true. Further, these functions predict that the accuracy of the conventional theories drops off quickly for oxides with intermediate thickness between 0.2 to 1 nm. For a monolayer oxide ($t = 0.15\,nm$), the deviation from the true contact area is 98% for the Sharvin equation and 99% for tunneling theory.

The feasibility of using these functions to correct contact area measurements was tested by comparing predictions to previous experimental observations. First, recent experiments using transmission electron microscopy (TEM) of a conductive Pt probe showed that contact area was 95% smaller than predicted by the Sharvin equation and proposed this was due to the presence of a 0.23 nm thick insulating layer, where the thickness was estimated from the resolution of the TEM[135]. Eq. 4.4(a) predicts that the difference between the true area and Sharvin calculation for an oxide of this thickness should be 99%, approximately consistent with the 95% deviation obtained in the experiment. Also, for an approximately 1.5-nm film, experimental measurements showed that the electrical contact area was less than 10% of the physical contact area estimated using continuum contact mechanics[162]. This observation correlates to over 90% difference between physical area and that measured from conductance, which is consistent with the model prediction of 99% for a 1.5 nm film.

This study has shown that the Sharvin equation for ballistic transport can be used to calculate contact area from conductance if there is no insulating layer (or a layer assumed to be less than ~0.1 nm thick) and tunneling theory applies for insulating layers thicker than approximately 1 nm. However, for a contact with an insulating layer between these limits, neither theory is expected to provide accurate results. However, in this intermediate range, the functions proposed here can be used to correct results obtained using the Sharvin or tunneling theories. For example, if the thickness of an insulating film is measured or estimated, contact area can be calculated from conductance using tunneling theory and then corrected using Eq. 4.4(b). Although the correction factors were developed using data for loads up to only tens of nanonewtons, we observe no statistically significant trend in c_S or c_T with load, so anticipate that they will be applicable to higher loading conditions. Therefore, this approach should provide a better measure of contact area than the typical approach of simply assuming ballistic transport using the Sharvin equation.

4.4 Conclusions

This study investigated the effect of oxide thickness on the contact area that is obtained from conductive AFM. Seven models of platinum tips were created with oxide thicknesses varying from 0 nm (no oxide) to 1.22 nm. The conduction between the tip and the substrate was approximated by identifying atomic channels across the oxide layer, where the conduction through each channel was computed using a DFT-derived current-separation relationship, which accounts for both direct metallic conduction and tunneling conduction. We found that the total conductance dropped rapidly with increasing oxide thickness due to the increasing contribution of tunneling and decreasing contribution of direct metallic conduction. To mimic a c-AFM measurement, the *computed* contact area was obtained from this conductance using a simple application of the Sharvin equation and/or tunneling theory. This computed contact area was compared with the *true* contact area calculated from atom positions at the contacting interface. The difference between the *computed* and *true* values of contact area was analyzed as a function of oxide thickness. The Sharvin equation for ballistic conduction was accurate for the case with no oxide, while tunneling theory provided accurate results for the thickest oxides tested. However, for oxides between 0.2 and 1 nm thick, both theories significantly underpredicted the contact area. This regime of oxide thickness is important for real-world devices because pure platinum typically contains a native surface oxide layer that has been estimated to be less than 0.5 nm thick.[135, 139] However, to develop a correction factor for contact area measurements more generally, additional studies will be needed. First, DFT data for conductance through platinum atom channels with oxygen will enable a more accurate empirical model for atom-atom conductance to be developed. Second, simulations of a wider range of tip sizes and loading conditions can capture more possible experimental conditions. Regardless, this work presents a framework for developing predictive models for contact area. Importantly, the results shown here emphasize that significant error may be associated with estimating contact area in c-AFM using conventional approaches, even for noble metals with only slight (sub-monolayer) coverage of surface layers.

Chapter 5 Pressure-dependence of work of adhesion at the nanoscale

5.1 Introduction

Adhesion is governed by atomic-scale interactions between surfaces, including van der Waals attraction, electrostatic interactions, and covalent bonding. These effects are typically captured by the work of adhesion W_{adh}, the energy required per unit area to separate two flat surfaces[163]. This property is fundamental to mechanics models that describe the contact between bodies[50]. Models based on adhesive spheres[12, 13, 15], and other, more-complex geometries[43, 164, 165] are widely used to predict surface properties of nanoscale contacts in scientific investigations and technological applications[166–168].

The assumption underlying these models is that the work of adhesion between the surfaces of the bodies remains constant. Recent work has suggested that this may not be the case and, instead, work of adhesion may depend on the loading conditions. Milne *et al.*[59] conducted nanoscale sliding and pull-off experiments to show that work of adhesion increases with stress and with speed of sliding prior to pull-off. In particular, it was shown that the measured work of adhesion is a result of a constant contribution due to van der Waals interactions, a term due to interfacial covalent bonding, and an extra term which increases with stress and the smoothness of the sliding probe. Complementary molecular dynamics simulations using silicon probes and diamond substrates revealed that adhesion is impacted by plastic rearrangements in the probe during sliding, i.e., smoothing, and by the presence of probe-substrate covalent bonds at the time of probe pullback[59]. Furthermore, the simulations showed that hydrogen termination of the diamond, applied load, sliding distance, and initial probe roughness all impact the simulated adhesion. Another recent study[60] examined the contact size of a silicon probe on diamond during loading and unloading and showed how the loading data could only be fit using a value of work of adhesion that increased with load up to the maximum force that was applied. Here, we use simulation study to characterize the variation of work of adhesion with applied pressure for nanoscale silicon/diamond contacts use and compare with extensive experiment. All the experimental data in this chapter are provided by Professor Tevis Jacobs' research group in University of Pittsburgh. Single-asperity adhesion tests at varying loads using nanoscale silicon probes against flat diamond surfaces were simulated using and molecular dynamics (MD) simulation.

5.2 Methods

5.2.1 Molecular dynamics simulations

Molecular dynamics simulations were used to model nanocontacts of the same material system as the experiments. A schematic of the atomistic model is shown in Fig. 5.1a and a representative force-time curve is shown in Fig. 5.1b. A parabolic silicon probe was created with a radius of 3 nm and was fully terminated with hydrogen. A Nosé-Hoover thermostat was applied to control the temperature of the system at 300 K. All interactions were

modeled by the ReaxFF potential[169] with the parameter set from Ref. [170] using a time step of 0.25 fs. The force was calculated as the sum of the forces on the probe atoms[40]. The probe moved towards the substrate at 5 m/s until it reached the desired force, remained at this position until the energy reached steady state, and then retracted from the substrate at 5 m/s. The simulation loading/unloading speed was much faster than that in the experiments due to the small timestep required by the atomistic simulation method. The maximum forces in the simulation ranged from 3 to 150 nN, resulting in a range of mean applied pressures from 3 to 11 GPa, consistent with the applied pressures in the experiments. Simulations were carried out using the large-scale atomic/molecular massively parallel simulator (LAMMPS)[171].

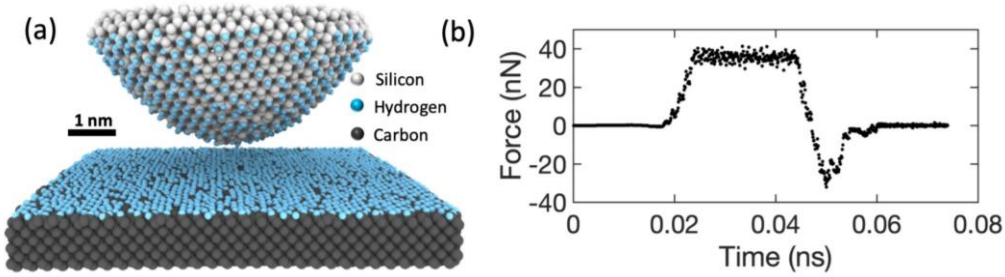

Figure 5.1 The adhesion tests were performed using atomistic simulations. Molecular dynamics simulations with a paraboloidal silicon probe and a flat diamond substrate (a), were used to measure force during loading and pull-off (b).

5.2.2 Calculation of the mean applied pressure using the elastic-plastic model

The elastic-plastic model of Kogut and Etsion [172] is used to measure the mean applied pressure at the maximum force for all the tests. This model is an extension of the Hertz model, to describe behavior after the body is predicted to exhibit local plastic deformation.

In this model, the transition from the elastic to elastic-plastic (yielding inception) occurs at the critical interference (deformation) ω_c. At the transition, the critical pressure p_c is calculated as $p_c = \frac{2}{3}KH$, where H is the hardness, K is a hardness coefficient that is calculated as K=0.454+0.41ν, and ν is the Poisson Ratio. For silicon, which has a Poisson ratio of 0.28 and a hardness of 13 GPa[173], the calculated critical pressure is 4.9 GPa.

Using the Hertz model, the normalized interference (ω/ω_c) can be related to the normalized pressure (p_h/p_c) by:[172]

$$\frac{\omega}{\omega_c} = \left(\frac{p_h}{p_c}\right)^2 \tag{5.1}$$

The mean Hertz pressure p_h at the maximum force F_{max} for a given probe radius R is given by:[69]

$$p_h = \frac{2}{3}\left(\frac{6F_{max}E_{eff}^2}{\pi^3 R^2}\right)^{1/3} \quad (5.2)$$

where $E_{eff} = \left[\frac{(1-\upsilon_1^2)}{E_1} + \frac{(1-\upsilon_2^2)}{E_2}\right]^{-1}$ is the effective modulus and E is the elastic modulus, and subscripts 1 and 2 refer to the two materials in contact.

For $\frac{\omega}{\omega_c} < 1$, the applied pressure is less than the critical pressure (4.9 GPa), and the contact is purely elastic. In this case, the mean pressure p_m is given by the mean Hertz pressure (Eq. 5.3).

For applied pressures greater than 4.9 GPa, the contact transitions into elastic-plastic and the mean pressure is given by the following empirical equations:[172]

For $1 \leq \frac{\omega}{\omega_c} \leq 6$, which corresponds to the prediction of the local yielding just below the surface with the contact being elastic, the mean pressure is given by:[172]

$$p_m = 1.1075 \times p_c \times \left(\frac{\omega}{\omega_c}\right)^{0.289} \quad (5.3)$$

For $6 \leq \frac{\omega}{\omega_c} \leq 110$, which corresponds to the global yielding with the contact area being elastic-plastic for $6 \leq \frac{\omega}{\omega_c} \leq 68$ and fully plastic for $68 \leq \frac{\omega}{\omega_c} \leq 110$, the prediction for the mean pressure is given by:[172]

$$p_m = 1.4894 \times p_c \times \left(\frac{\omega}{\omega_c}\right)^{0.1170} \quad (5.4)$$

5.3 Results and discussion

Previous work on nanoscale diamond contacts showed that the work of adhesion depends on the hydrogen coverage[59, 174–176]. Because the termination of the experimental surfaces was unknown, the flat diamond substrate was investigated at hydrogen coverages ranging from 0 to 100%. The adhesion results are shown in Fig. 5.2. The surface termination was chosen to most closely match the work of adhesion measured in the experiments, where the precise surface termination is unknown. A coverage of 85% was chosen for this study to best match the experimental results in terms of the magnitude of the work of adhesion.

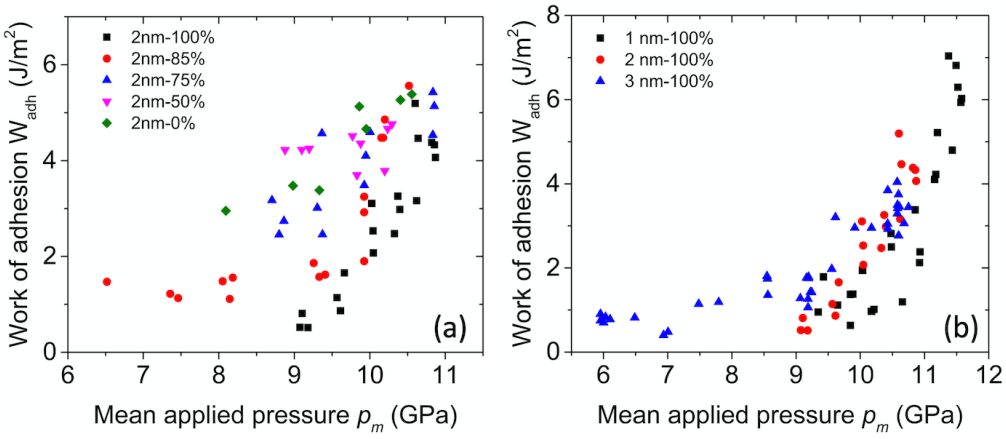

Figure 5.2 The work of adhesion from the simulation varied with increasing hydrogen coverage (a), consistent with prior results[176], but data from all coverages exhibited increasing trends with applied pressure. Work of adhesion was also measured with three different probe sizes (b) with a hydrogen coverage of 100% and the trends in work of adhesion were again consistent.

The work of adhesion W_{adh} was computed using the Maugis-Dugdale model of adhesive contact from the adhesive force F_{adh} as:[177]

$$W_{adh} = \frac{F_{adh}}{\chi \pi R} \tag{5.5}$$

where χ is a dimensionless parameter ranging from 1.5 to 2. The adhesive force F_{adh} was measured as the maximum adhesive force during pull off from the force-time data in the simulation (Fig. 5.1b). The radius R of the apex of the probe was measured before and after the test by tracing the outer contour of the probe from the high-resolution TEM image or side view of the atom positions in the simulation, and the extracted profile was fit with a parabola of form $z = x^2/2R$, where z is the vertical height and x is the lateral dimension.

The value of χ in Eq. 5.5 depends on the nature of contact. Its limits correspond to the Derjaguin–Müller–Toporov (DMT) model[12] (χ = 2), which assumes weaker and longer-range adhesive interactions and is applicable for stiffer materials, and the Johnson-Kendall-Roberts (JKR) model[13] (χ = 1.5), which assumes short-range adhesion and is applicable for softer materials. To determine its value, we used the model of Maugis[15] and the numerical method of Carpick-Ogletree-Salmeron (COS)[177]. The Maugis parameter[15] was calculated as:

$$\lambda = 2\sigma_0 \left(\frac{9R}{16\pi E_{eff}^2 W_{adh}} \right)^{1/3} \tag{5.6}$$

where σ_0 is the theoretical cohesive stress and z_0 is the equilibrium separation between the materials. The cohesive stress σ_0 was determined by equating it to the minimum adhesive stress of the Lennard-Jones potential, which gives $\sigma_0 = W_{adh}/0.97z_0$.[177] For a silicon-diamond contact, the equilibrium separation z_0 is 0.25 nm[9, 37, 73, 178, 179] and the

effective modulus E_{eff} is 124.5 GPa, calculated from the elastic modulus of [1 0 0] diamond (E = 1050.0 GPa, ν = 0.1)[77] and [1 0 0] silicon (E = 130 GPa, ν = 0.28).[78] Using these values of z_0 and E_{eff}, and the vales of F_{adh} and R measured in the experiments and simulations, the COS method was applied to simultaneously measure the Maugis parameter λ and work of adhesion W_{adh} for all the tests. It was observed that the Maugis parameter λ lies in the range of 0.23−1.56, thus representing an intermediate case between the DMT and JKR limits. All reported work of adhesion values were subsequently determined based on this implementation of the Maugis-Dugdale model.

The results from the adhesion tests are shown in Fig. 5.3. Together, the experimental and simulation data show an increase in work of adhesion from approximately 1 J/m^2 at zero applied pressure up to 6-8 J/m^2 at high pressures. The increase is gradual at low pressures where deformation is expected to be elastic and then increases rapidly at the higher pressures of elastic-plastic deformation. The results at zero applied pressure agree well with those of Ref. [59], in which sliding and pull-off experiments were conducted under the action of adhesive stress only. Simulations performed in that study with Si probes and diamond surfaces showed that larger loads increased smoothing of the probe and interfacial covalent-bond formation, both of which increase adhesion. The present results show that the work of adhesion continuously increases with applied pressure up to very high values. Simulated testing with other probe sizes and other hydrogen coverages (Fig. 5.2) show that, while the absolute values of work of adhesion vary between conditions, the trends of increasing work of adhesion with applied pressure are consistent across all simulated contacts.

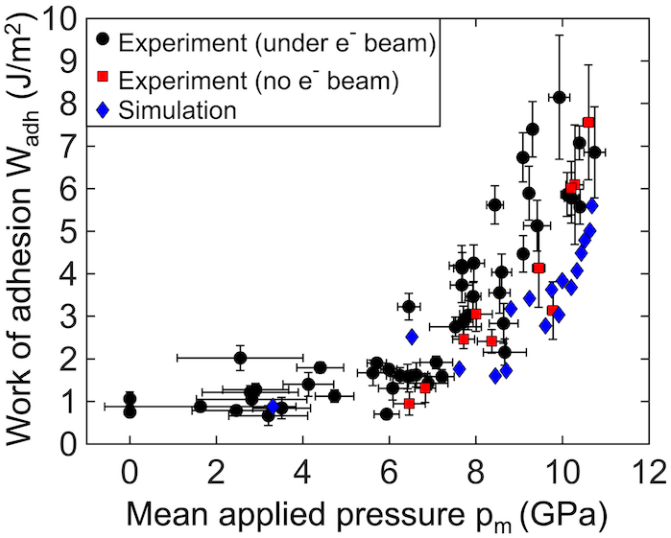

Figure 5.3 The measured work of adhesion from experiments and simulations increases approximately seven-fold with applied pressure, where the most significant increase occurs above 5 GPa. The work of adhesion is calculated using the Maugis-Dugdale model; the mean applied pressure is calculated using an elastic-plastic model of contact. Experimental data is provided by Professor Tevis Jacobs' research group in University of Pittsburgh.

These results demonstrate a significant increase in work of adhesion with applied pressure. To support that these changes arise from atomic bonding, rather than other physical origins, we sought to rule out other common explanations for varying adhesion, including: shape change by inelastic deformation[180] (such as fracture or gross plastic flow); and time-dependent deformation[22–24] (such as viscoelasticity or creep).

First, while large-scale shape change from inelastic deformation (fracture or gross plastic flow) could potentially lead to an increase in contact size and therefore adhesive force, this was ruled out by examining the probes before and after testing. From side-view images of the probes, the exterior profile was extracted and a parabola was fit to the probe's apex (see Fig. 5.4 a,c). In all cases, the average change in radius of the probe apex was just 1%, with no single radius deviating by more than 9% from the pre-test value. To assess any smaller-scale changes, the best-fit parabola was subtracted from the measured profile leaving only the sub-nm-scale roughness. In all cases, the roughness was approximately equivalent before and after testing: the average change in root-mean-square (RMS) roughness of all the probes was 1%, with no single value of RMS roughness deviating by more than 9% from the pre-test value. Furthermore, images of the probes taken immediately after testing (Fig. 5.4 b,d) showed no evidence of dislocations or other defects in the crystal lattice.

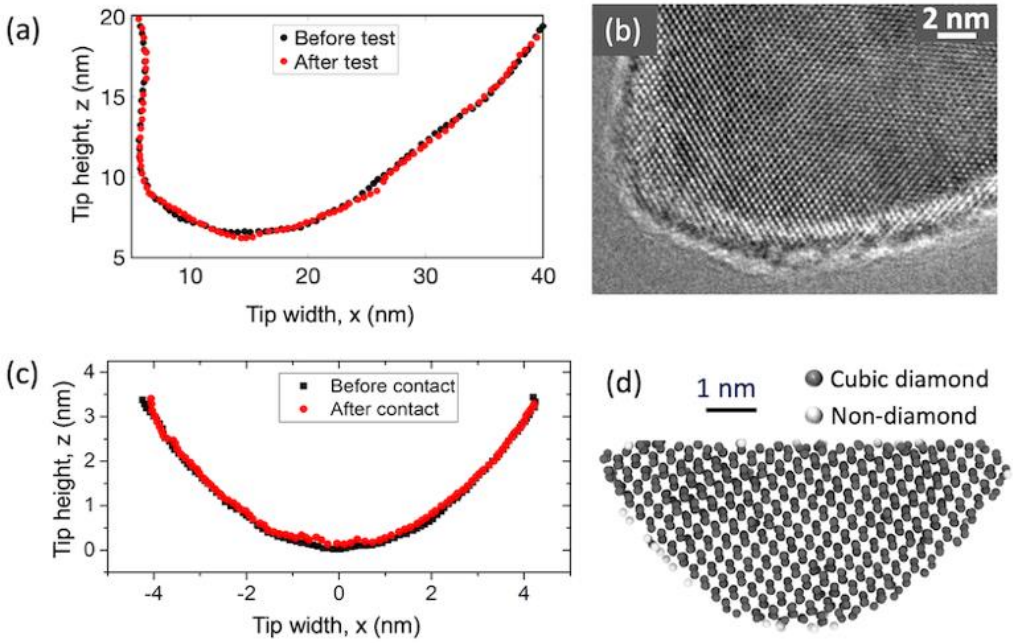

Figure 5.4 The increase in work of adhesion with applied pressure is not due to the shape change by inelastic deformation. Comparison of the probe shapes before and after the test suggest no significant shape change in both the experiments (a) and simulations (c). TEM images of the probes (b) and crystallographic analysis of the model (d) after the test showed no evidence of defects in the silicon lattice. Experimental data is provided by Professor Tevis Jacobs' research group in University of Pittsburgh.

Second, to rule out time-dependent phenomena such as creep or viscoelasticity, the adhesion tests were repeated with variation in hold time and pull-off rate. Simulation tests were conducted for different hold times from 2 to 12 ns at three maximum forces of 132.2 $\pm$ 2.0, 21.8 $\pm$ 0.8, and 2.2 $\pm$ 0.4 nN. Similarly, experimental tests were conducted for five different hold times. The adhesive force showed no significant trends with hold time in both experiments (Fig. 5.5 a) and simulations (Fig. 5.5 b). Further, the contact tests were conducted at different rate of pull-off was varied from 2 to 10 m/s. The pull-off force did not show any significant change with unloading rate in the range of 0 to 2 nm/s in the experiment (Fig. 5.5 c) and in the simulations (Fig. 5.5 d). Therefore, the tested range of hold times and speeds had no effect on measured adhesion and cannot explain the increase of work of adhesion with applied pressure.

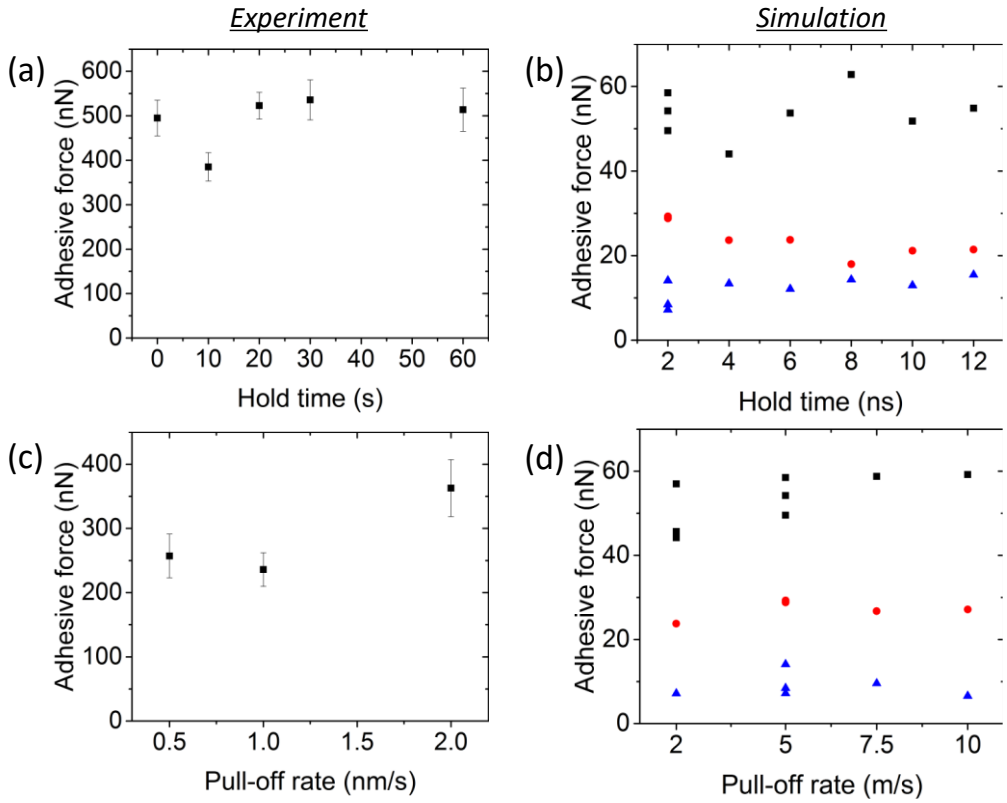

Figure 5.5 The increase in work of adhesion with applied pressure is not due to time-dependent phenomena. In both experiments (a,c) and simulations (b,d), the adhesive force shows no dependence on hold time nor pull-off rate, and hence, time-dependent flow such as creep or viscoelasticity can be ruled out. In (b) and (d), the black squares, red circles, and blue triangles refer to maximum applied forces of 132 nN, 21.8 nN, and 2.2 nN, respectively, for a probe radius of 3 nm. Although the timescales of the experiment and simulation differ significantly, these plots confirm that the adhesive force does not depend on the hold time or pull-off rate within the range of times and rates accessible to each method. Experimental data is provided by Professor Tevis Jacobs' research group in University of Pittsburgh.

Since the possible effect of the common explanations for varying adhesion—shape change by inelastic deformation, and time-dependent deformation—were excluded, the present results are attributed to chemical bonding across the interface that is facilitated by stress as suggested by prior experiments and MD simulations[59, 60]; we show that these trends continue and are accelerated with applied pressure. Specifically, the increase in measured work of adhesion corresponds to a stress-driven increase in interfacial bond density, requiring a larger energy per unit area to separate the surfaces. TEM images before and after contact were compared and no material transfer was identified within the detection limits of the instrument (0.2 nm on the probe based on the TEM resolution and 1 nm on the diamond based on vibration of the indenter). Additionally, there was not more than a few atoms of material transfer in the simulated testing. Therefore, while the bond density appears to increase with applied load, the separation of the bodies still occurs at the original interface between the materials.

5.4 Conclusions

In summary, this study quantified the increase of the work of adhesion between silicon and diamond with externally applied pressure. Using compression-and-adhesion tests performed on well-controlled silicon-diamond interfaces inside a TEM and complementary atomistic simulations, we found that the strength of adhesion increases with applied pressure. After systematically ruling out other explanations for varying work of adhesion, the increase is attributed to changes in atomic bonding across the interface. This effect causes a seven-fold increase in adhesion with externally applied pressures up to 11 GPa. In general, the findings reported here support newer models of contact, in which the work of adhesion is not represented as a static property of the interface, but instead as having a well-defined functional dependence on applied pressure.

Chapter 6 Summary and future work

6.1 Summary

Contact area and adhesion at the nanoscale were investigated using molecular dynamics simulations designed to complement experimental measurements.

First, a contact between a silicon tip and a diamond flat surface was simulated with a model that matched experiment, including materials, geometry, structure, crystal orientation and applied force. Further, the adhesion of the interface was tuned using the Buckingham potential to reproduce the value observed in the experiment. The contact area was then computed by (a) identifying the contact atoms; and (b) converting contact atoms to contact area. The contact atoms were identified using a distance criterion or a force criterion. The contact area was then computed as atomic or apparent area. The results demonstrated that the choice of method for computing contact area can lead to significant variations in measured results. Further, variation of contact area during loading and unloading was observed. Such variation cannot be explained by the continuum theories, which suggests the failure of continuum theories to describe a complete contact process.

Next, contact area can be determined from electron transport theories for conductive contacts. To evaluate this method, atomistic simulations were used to model metallic contact of a platinum tip and a platinum flat surface with matched conditions as mentioned above. The contact area computed from the simulations was then compared with the measurements from the conductance and electron transport theories of the same conductive test. The application of electron transport theories to the measured conductance yielded measurements of contact size that were 95% smaller than the simulation values. The physical mechanism for this deviation from electron transport theories was shown to be due to the presence of monolayer insulating surface species that either reduced the metal-metal contact area or eliminated it entirely, requiring tunneling.

To further understanding the contribution of monolayer insulating species on metallic conduction, different models of platinum tips were created with oxide thicknesses varying from 0 nm (no oxide) to 1.22 nm. The conduction between the tip and the substrate was approximated by identifying atomic channels across the oxide layer, where the conduction through each channel was computed using a DFT-derived current-separation relationship, which accounts for both direct metallic conduction and tunneling conduction. We found the total conductance dropped rapidly with increasing oxide thickness due to the increasing contribution of tunneling and decreasing contribution of direct metallic conduction. The results demonstrated that the ballistic model of the electron transport theories was accurate for the case with no oxide, while tunneling theory provided accurate results for the thickest oxides tested. However, for oxides between 0.2 and 1 nm thick, both theories significantly underpredicted the contact area. A correction of the electron transport theories is needed to describe conduction where there is a sub-nm insulating layer on the contact surface.

Finally, the strength of adhesion between surfaces, which significantly affects contact area at the nanoscale, was investigated. We tested the hypothesis that work of adhesion is constant for a given material pair with a silicon and diamond contact. Results showed that work of adhesion increased with applied pressure. After ruling out other explanations for varying work of adhesion, such as inelastic deformation and time-dependent material creep, we proposed the increase was attributed to changes in atomic bonding across the interface.

6.2 Future Work

6.2.1 Limits of the applicability of continuum contact mechanics models

Continuum contact mechanics models have been used to describe contact at the nanoscale using AFM experiments [16, 19–21]. However, these experiments are typically limited to specific conditions and certain materials. Continuum contact mechanics models may break down at the nanoscale due to the surface roughness [44, 45] or reversible plasticity [181, 182]. Also, Chapter 2 showed continuum contact mechanics models fail to predict the adhesion hysteresis behavior for contact bodies approaching and separating. However, despite evidence of a breakdown of contact mechanics models at the nanoscale, these models are still widely used in both basic science and engineering applications. Therefore, further investigation is required to determine under what conditions continuum contact mechanics models can be applied to calculate contact properties.

Continuum contact mechanics models relate the contact area with geometry of contact bodies, material properties and the applied load. The DMT, JKR, or Maugis-Dugdale models describe the contact of spherical bodies [147], and they have also been extended to non-spherical geometries by describing the behavior of bodies with the shape of an analytical power-law function of arbitrary exponent [183]. Regarding the size of the contact bodies, previous studies have found the continuum models may underestimate the contact area at small loads and this underestimate decreases with increasing load and radius of contact bodies [44]. Other experimental studies have also demonstrated continuum theories could be used to describe contact for radius of contact bodies over 100 nm [19, 20]. For the effect of the properties of the contact bodies, DMT model is applicable for stiff materials with weak and long-range adhesion, while JKR model is suitable for soft materials with strong and short-range adhesion. However, previous research suggests that some metallic materials, like gold or silver, exhibit cold-welding or liquid-like behaviors at contact [184, 185], which could not be described by continuum theories. Further, recent studies have shown that reversible plasticity may cause deviations from the predictions of continuum elasticity [181, 182]. Therefore, to determine the limits of continuum models at the nanoscale in term of geometry of contact bodies, materials, and applied load, we propose future research using the contact models described below.

First, we propose models consisting of atomically smooth, hemispherical bodies to eliminate the geometry and roughness effects. Surface roughness has been found to affect the predictions of contact pressure and area by continuum theories [44, 45]. Second, to test

the tip size effect, tips with different radii will be modeled and the radius ranges from 1 nm to 100 nm. This range of the tip radius covers range of realistic experimental tips. Regarding the materials of the contacting bodies, cold-welding materials (gold, silver) should be avoided, so ideal starting materials are silicon and diamond. These materials have relatively large elasticity modulus to retain elasticity at large applied force and also have been widely studied. Further, the contact bodies should be be fully passivated to minimize adhesion hysteresis resulting from bonding across the contact. The area-load relation can be analyzed and compared the results with continuum mechanics predictions. We hypothesize that the area from MD simulations will be consistent with continuum models for larger tips and small loads, but continuum contact mechanics will fail for smaller tips and higher loads. Results will be analyzed to identify the limits of the continuum mechanics models in terms of a range of the tip size, and the responding maximum applied stress.

6.2.2 Origin of load dependence of contact and work of adhesion

Continuum mechanics models assume a constant interfacial energy, or work of adhesion. However, as reported in Chapter 4, the work of adhesion increases with the applied load. The changing work of adhesion is typically attributed to capillary effects [22] or to viscoelasticity in soft material [23, 24], or to plastic deformation [80]. However, these factors have been ruled out and the hypothesis of reversible dislocations and stress-driven chemical reactions in the contact has been proposed.

Recent studies of contact between a platinum tip and a platinum surface have demonstrated that contact softening leads to a larger contact area than continuum predictions due to a fully-reversed dislocation activity caused by the discrete surface steps at the interface [181, 182]. This reversible plasticity increases the contact area above the fully elastic predictions for a stepped surface and then requires larger force to separate the contact. It has also been experimentally observed that pull-off forces are often strongly dependent on the maximum applied load [186]. This is typically attributed to an increase in the area of contact between the bodies. In soft materials, this is explained by flow of the soft material, to achieve more complete contact [187–189] with the other side. In hard materials, this is explained by an increase in the area of contact due to inelastic deformation – either of the global geometry of the bodies [80] or of the surface roughness [190–192]. Therefore, this results in a larger contact area and then stronger interaction in the separation process than in the approach process, which would lead to a larger work of adhesion.

Previous research has also shown that contact aging-which describes the phenomenon where contact area increases with the time that the two surfaces are held in contact-would result in a larger contact area at the separation process. This contact aging has been attributed to asperity creep [193, 194] and to thermally activated bond formation across the interface [195] and which leads to a stronger interaction across the interface. Therefore, we propose that the increasing work of adhesion with applied load may be caused by a) reversible plasticity at loading and/or b) changes in the strength of the interactions across the interface as the contact is loaded. To access the reversible plasticity effect, we will monitor and analyze the dislocations at the contact interface and relate them with the

applied load and contact properties. For the variation of strength of the interaction, it is represented by work of adhesion. This variation of the work of adhesion may be explained by increased formation of bonds across the interface. This would correspond to an increase in the energy required to separate that unit of area. Therefore, further study using a reactive potential will be needed to fully understand the formation and breaking of bonds across the contact.

To address these questions, we suggest simulation of contact models with different material pairs to further confirm the present of load dependent work of adhesion. The dislocations and covalent bonds across the interface can be characterized at different applied loads. The dislocation length and bond density at the interface can be correlated to work of adhesion as well as contact area. Finally, the simulations can be used to identify a mechanism that explains the origin of the load dependence of work of adhesion.

6.3 Concluding Remarks

This dissertation has (a) demonstrated simulations methods for defining and computing nanoscale contact properties using atomistic simulations, (b) quantified the limitations of continuum mechanics models for nanoscale contacts, and (c) shown that the work of adhesion, which was previously assumed to be a material property, is dependent on applied load.

Contact properties are important for engineering applications and basic science, but their measurement is challenging and requires use of continuum theories. The assumptions underlying those theories may break down and cause inaccurate measurement of the contact properties at the nanoscale. With the methods developed in this dissertation, the applicability and of such continuum theories can be determined, which will improve the accuracy of the nanoscale contact property estimates and thus reliability of contact measurements and calculations.

Further, the work of adhesion is an important characteristic for nanoscale surfaces. For example, the operation of nanoswitches mainly relies on the work of adhesion of the contact surfaces and such work of adhesion is usually measured by atomic force microscopes with the assumption that the work of adhesion is a constant. However, our results suggest that the work of adhesion depends on the externally applied load. This means AFM-based measurement of work of adhesion may result in different values when measured at different loads. This inconsistency can adversely affect the function of nanoscale devices such as nanoswitches. However, the methods developed here can be used to understand why adhesion changes with load and account for that during design.

Overall, this dissertation has defined contact at the nanoscale and demonstrated limits of continuum theories. The findings will benefit both engineering applications and basic science. First, the resolution, accuracy, and reliability of nanoscale applications, including scanning probe microscopy, probe-based nanomanufacturing and nanodevices, depend on the contact properties, e.g. contact area and adhesion. Second, fundamental studies of friction, wear, and transport phenomena at the nanoscale rely on the measurement of the

contact properties at the nanoscale. Third, the principal of contact at larger scales can be better explained with a fundamental understanding of contact at the nanoscale.

References

1. Chou, S.Y., Krauss, P.R., Renstrom, P.J.: Imprint of sub-25 nm vias and trenches in polymers. Appl. Phys. Lett. 67, 3114–3116 (1995).
2. Piner, R.D., Zhu, J., Xu, F., Hong, S., Mirkin, C.A.A.: "Dip-Pen" Nanolithography. Science (80-.). 283, 661–663 (1999).
3. Kim, T.-H., Chung, D.-Y., Ku, J., Song, I., Sul, S., Kim, D.-H., Cho, K.-S., Choi, B.L., Kim, J.M., Hwang, S., Kim, K.: Heterogeneous stacking of nanodot monolayers by dry pick-and-place transfer and its applications in quantum dot light-emitting diodes. Nat. Commun. 4, 2637 (2013).
4. Majumdar, A.: SCANNING THERMAL MICROSCOPY. Annu. Rev. Mater. Sci. 1999. (2003).
5. Park, J.Y., Maier, S., Hendriksen, B., Salmeron, M.: Sensing current and forces with SPM. Mater. Today. 13, 38–45 (2010).
6. Rebeiz, G.M., Muldavin, J.B.: RF MEMS switches and switch circuits. IEEE Microw. Mag. 2, 59–71 (2001).
7. Loh, O.Y., Espinosa, H.D.: Nanoelectromechanical contact switches. Nat. Nanotechnol. 7, 283–295 (2012).
8. Lantz, M.A., O'Shea, S.J., Welland, M.E.: Simultaneous force and conduction measurements in atomic force microscopy. Phys. Rev. B. 56, 15345 (1997).
9. Enachescu, M., van den Oetelaar, R.J. a, Carpick, R.W., Ogletree, D.F., Flipse, C.F.J., Salmeron, M.: Atomic force microscopy study of an ideally hard contact: The diamond(111) tungsten carbide interface. Phys. Rev. Lett. 81, 1877–1880 (1998).
10. No Title.
11. Hertz, H.: On the contact of elastic solids. J. reine angew. Math. 92, 156–171 (1881).
12. Derjaguin, B. V, Muller, V.M., Toporov, Y.P.: Effect of contact deformations on the adhesion of particles. J. Colloid Interface Sci. 53, 314–326 (1975).
13. Johnson, K.L., Kendall, K., Roberts, A.D.: Surface Energy and the Contact of Elastic Solids. Proc. R. Soc. London A Math. Phys. Eng. Sci. 324, 301–313 (1971).
14. Tabor, D.: Surface forces and surface interactions. J. Colloid Interface Sci. 58, 2–13 (1977).
15. Maugis, D.: Adhesion of spheres: The JKR-DMT transition using a dugdale model. J. Colloid Interface Sci. 150, 243–269 (1992).
16. Carpick, R.W., Ogletree, D.F., Salmeron, M.: A General Equation for Fitting Contact Area and Friction vs Load Measurements. J. Colloid Interface Sci. 211, 395–400 (1999).
17. Piétrement, O., Troyon, M.: General Equations Describing Elastic Indentation Depth and Normal Contact Stiffness versus Load. J. Colloid Interface Sci. 226, 166–171 (2000).
18. Popov, V.L.: Contact mechanics and friction. In: Metal Machining. pp. 363–374. Springer (2013).
19. Carpick, R.W., Agraït, N., Ogletree, D.F., Salmeron, M.: Variation of the

Interfacial Shear Strength and Adhesion of a Nanometer-Sized Contact. Langmuir. 12, 3334–3340 (1996).
20. Enachescu, M., van den Oetelaar, R.J.A., Carpick, R.W., Ogletree, D.F., Flipse, C.F.J., Salmeron, M.: Atomic Force Microscopy Study of an Ideally Hard Contact: The Diamond(111)/Tungsten Carbide Interface. Phys. Rev. Lett. 81, 1877 (1998).
21. Carpick, R.W., Agraït, N., Ogletree, D.F., Salmeron, M.: Measurement of interfacial shear (friction) with an ultrahigh vacuum atomic force microscope. J. Vac. Sci. Technol. B. 14, 1289–1295 (1996).
22. de Boer, M.P., Knapp, J.A., Michalske, T.A., Srinivasan, U., Maboudian, R.: Adhesion hysteresis of silane coated microcantilevers. Acta Mater. 48, 4531–4541 (2000).
23. Attard, P.: Interaction and deformation of viscoelastic particles: Nonadhesive particles. Phys. Rev. E. 63, 61604 (2001).
24. Chen, Y.L., Helm, C.A., Israelachvili, J.N.: Molecular mechanisms associated with adhesion and contact angle hysteresis of monolayer surfaces. J. Phys. Chem. 95, 10736–10747 (1991).
25. Israelachvili, J.N.: Intermolecular and surface forces: revised third edition. Academic press (2011).
26. Agraït, N., Yeyati, A.L., van Ruitenbeek, J.M.: Quantum properties of atomic-sized conductors, (2003).
27. Gotsmann, B., Lantz, M.A.: Quantized thermal transport across contacts of rough surfaces. Nat. Mater. 12, 59–65 (2013).
28. Kopycinska-Müller, M., Geiss, R.H., Hurley, D.C.: Contact mechanics and tip shape in AFM-based nanomechanical measurements. Ultramicroscopy. 106, 466–474 (2006).
29. Carpick, R.W., Ogletree, D.F., Salmeron, M.: Lateral stiffness: A new nanomechanical measurement for the determination of shear strengths with friction force microscopy. Appl. Phys. Lett. 70, 1548–1550 (1997).
30. Jacobs, T.D.B., Ryan, K.E., Keating, P.L., Grierson, D.S., Lefever, J.A., Turner, K.T., Harrison, J.A., Carpick, R.W.: The effect of atomic-scale roughness on the adhesion of nanoscale asperities: A combined simulation and experimental investigation. Tribol. Lett. 50, 81–93 (2013).
31. Jacobs, T.D.B., Carpick, R.W.: Nanoscale wear as a stress-assisted chemical reaction. Nat. Nanotechnol. 8, 108–112 (2013).
32. Nanoscale wear as a stress-assisted chemical reaction. Nat. Nanotechnol. 8, 108 (2013).
33. Jacobs, T.D.B., Lefever, J.A., Carpick, R.W.: A Technique for the Experimental Determination of the Length and Strength of Adhesive Interactions Between Effectively Rigid Materials. Tribol. Lett. 59, 1 (2015).
34. Jacobs, T.D.B., Lefever, J.A., Carpick, R.W.: Measurement of the Length and Strength of Adhesive Interactions in a Nanoscale Silicon-Diamond Interface. Adv. Mater. Interfaces. (2015).
35. Alsem, D.H., Sood, S., Salmon, N., Jacobs, T.D.B.: In situ electrical testing of device-relevant nanocontacts in the transmission electron microscope. Microsc. Microanal. 22, 818–819 (2016).

36. Bradley, R.S.R.: The cohesive force between solid surfaces and the surface energy of solids. London, Edinburgh, Dublin Philos. Mag. J. Sci. 13, 853–862 (1932).
37. Grierson, D.S., Flater, E.E., Carpick, R.W.: Accounting for the JKR-DMT transition in adhesion and friction measurements with atomic force microscopy. J. Adhes. Sci. Technol. 19, 291–311 (2005).
38. Chandross, M., Lorenz, C.D., Stevens, M.J., Grest, G.S.: Simulations of nanotribology with realistic probe tip models. Langmuir. 24, 1240–1246 (2008).
39. Li, Q., Dong, Y., Perez, D., Martini, A., Carpick, R.W.: Speed dependence of atomic stick-slip friction in optimally matched experiments and molecular dynamics simulations. Phys. Rev. Lett. 106, (2011).
40. Ryan, K.E., Keating, P.L., Jacobs, T.D.B., Grierson, D.S., Turner, K.T., Carpick, R.W., Harrison, J.A.: Simulated adhesion between realistic hydrocarbon materials: effects of composition, roughness, and contact point. Langmuir. 30, 2028–2037 (2014).
41. Hu, X., Martini, A.: Atomistic simulations of contact area and conductance at nanoscale interfaces. Nanoscale. 9, 16852–16857 (2017).
42. Mo, Y., Szlufarska, I.: Roughness picture of friction in dry nanoscale contacts. Phys. Rev. B. 81, 35405 (2010).
43. Reedy, E.D.: Thin-coating contact mechanics with adhesion. J. Mater. Res. 21, 2660–2668 (2006).
44. Luan, B., Robbins, M.O.: The breakdown of continuum models for mechanical contacts. Nature. 435, 929–932 (2005).
45. Luan, B., Robbins, M.O.: Contact of single asperities with varying adhesion: Comparing continuum mechanics to atomistic simulations. Phys. Rev. E. 74, 26111 (2006).
46. Burnham, N.A., Colton, R.J., Pollock, H.M.: Interpretation issues in force microscopy. J. Vac. Sci. Technol. A. 9, 2548–2556 (1991).
47. Solhjoo, S., Vakis, A.I.: Definition and detection of contact in atomistic simulations. Comput. Mater. Sci. 109, 172–182 (2015).
48. Cheng, S., Robbins, M.O.: Defining Contact at the Atomic Scale. Tribol. Lett. 39, 329–348 (2010).
49. Cheng, S., Luan, B., Robbins, M.O.: Contact and friction of nanoasperities: Effects of adsorbed monolayers. Phys. Rev. E. 81, 16102 (2010).
50. Jacobs, T.D.B., Martini, A.: Measuring and understanding contact area at the nanoscale: a review. Appl. Mech. Rev. 69, 61101 (2017).
51. Erts, D., Olin, H., Ryen, L., Olsson, E., Tholen, A.: Maxwell and Sharvin conductance in gold point contacts investigated using TEM-STM. Phys. Rev. B. 61, 12725–12727 (2000).
52. Strange, M., Kristensen, I.S., Thygesen, K.S., Jacobsen, K.W.: Benchmark density functional theory calculations for nanoscale conductance. J. Chem. Phys. 128, 114714 (2008).
53. Nielsen, S.K., Noat, Y., Brandbyge, M., Smit, R.H.M., Hansen, K., Chen, L.Y., Yanson, A.I., Besenbacher, F., van Ruitenbeek, J.M.: Conductance of single-atom platinum contacts: Voltage dependence of the conductance histogram. Phys. Rev. B. 67, 245411 (2003).

54. García-Suárez, V.M., Rocha, A.R., Bailey, S.W., Lambert, C.J., Sanvito, S., Ferrer, J.: Conductance Oscillations in Zigzag Platinum Chains. Phys. Rev. Lett. 95, 256804 (2005).
55. Strange, M., Thygesen, K.S., Jacobsen, K.W.: Electron transport in a <math display="inline"> <mrow> <mi>Pt</mi> <mtext>−</mtext> <mi>CO</mi> <mtext>−</mtext> <mi>Pt</mi> </mrow> </math> nanocontact: Density functional theory calculations. Phys. Rev. B. 73, 125424 (2006).
56. Zotti, L.A., Pérez, R.: Platinum atomic contacts: From tunneling to contact. Phys. Rev. B. 95, 125438 (2017).
57. Onofrio, N., Strachan, A.: Voltage equilibration for reactive atomistic simulations of electrochemical processes. J. Chem. Phys. 143, 054109 (2015).
58. Yang, F., Carpick, R.W., Srolovitz, D.J.: Mechanisms of Contact, Adhesion, and Failure of Metallic Nanoasperities in the Presence of Adsorbates: Toward Conductive Contact Design. ACS Nano. 11, 490–500 (2017).
59. Milne, Z.B., Schall, J.D., Jacobs, T.D.B., Harrison, J.A., Carpick, R.W.: Covalent Bonding and Atomic-Level Plasticity Increase Adhesion in Silicon-Diamond Nanocontacts. ACS Appl. Mater. Interfaces. Accepted (2019).
60. Vishnubhotla, S.B., Chen, R., Khanal, S., Hu, X., Martini, A., Jacobs, T.D.B.: Matching atomistic simulations and in situ experiments to investigate the mechanics of nanoscale contacts. Tribol. Lett. 67, 97 (2019).
61. Cha, P.-R., Srolovitz, D.J., Kyle Vanderlick, T.: Molecular dynamics simulation of single asperity contact. Acta Mater. 52, 3983–3996 (2004).
62. Szlufarska, I., Chandross, M., Carpick, R.W.: Recent advances in single-asperity nanotribology. J. Phys. D. Appl. Phys. 41, 123001 (2008).
63. Mo, Y., Turner, K.T., Szlufarska, I.: Friction laws at the nanoscale. Nature. 457, 1116–1119 (2009).
64. Mo, Y., Szlufarska, I.: Roughness picture of friction in dry nanoscale contacts. Phys. Rev. B - Condens. Matter Mater. Phys. 81, 035405 (2010).
65. Rodrigues, V., Fuhrer, T., Ugarte, D.: Signature of Atomic Structure in the Quantum Conductance of Gold Nanowires. Phys. Rev. Lett. 85, 4124 (2000).
66. Rubio, G., Agraït, N., Vieira, S.: Atomic-sized metallic contacts: Mechanical properties and electronic transport. Phys. Rev. Lett. 76, 2302–2305 (1996).
67. Jacobs, T.D.B., Carpick, R.W.: Nanoscale wear as a stress-assisted chemical reaction. Nat. Nanotechnol. 8, 108–112 (2013).
68. Liu, J., Notbohm, J.K., Carpick, R.W., Turner, K.T.: Method for characterizing nanoscale wear of atomic force microscope tips. ACS Nano. 4, 3763–3772 (2010).
69. Johnson, K.L., Keer, L.M.: Contact Mechanics. J. Tribol. 108, 659 (1986).
70. Dong, Y., Li, Q., Martini, A.: Molecular dynamics simulation of atomic friction: A review and guide. J. Vac. Sci. Technol. A. 31, 30801 (2013).
71. Plimpton, S.: Fast parallel algorithms for short-range molecular dynamics. J. Comput. Phys. 117, 1–19 (1995).
72. Kumagai, T., Izumi, S., Hara, S., Sakai, S.: Development of bond-order potentials that can reproduce the elastic constants and melting point of silicon for classical molecular dynamics simulation. Comput. Mater. Sci. 39, 457–464 (2007).
73. Jacobs, T.D.B., Lefever, J.A., Carpick, R.W.: Measurement of the Length and

Strength of Adhesive Interactions in a Nanoscale Silicon–Diamond Interface. Adv. Mater. Interfaces. 2, 1400547 (2015).
74. Guo, Q., Izumisawa, S., Phillips, D.M., Jhon, M.S.: Surface morphology and molecular conformation for ultrathin lubricant films with functional end groups. J. Appl. Phys. 93, 8707–8709 (2003).
75. Yi, T., Ramasamy, U.S., Lichter, S., Martini, A.: Stability and structure of nanometer-thin perfluoropolyether films using molecular simulations. Tribol. Lett. 54, 119–127 (2014).
76. Huheey, T.L.: Cottrell, The Strengths of Chemical Bonds, (1958).
77. McSkimin, H.J., Andreatch Jr, P.: Elastic Moduli of Diamond as a Function of Pressure and Temperature. J. Appl. Phys. 43, 2944–2948 (1972).
78. Hopcroft, M.A., Nix, W.D., Kenny, T.W.: What is the Young's Modulus of Silicon? J. Microelectromechanical Syst. 19, 229–238 (2010).
79. SHARVIN, Y. V: A Possible Method for Studying Fermi Surfaces. Sov. Phys. Jetp-Ussr. 21, 655- (1965).
80. Horn, R.G., Israelachvili, J.N., Pribac, F.: Measurement of the deformation and adhesion of solids in contact. J. Colloid Interface Sci. 115, 480–492 (1987).
81. Eckmann, A., Felten, A., Mishchenko, A., Britnell, L., Krupke, R., Novoselov, K.S., Casiraghi, C.: Probing the nature of defects in graphene by Raman spectroscopy. Nano Lett. 12, 3925–3930 (2012).
82. Brown, B.P., Picco, L., Miles, M.J., Faul, C.F.J.: Conductive-AFM Patterning of Organic Semiconductors. Small. 11, 5054–5058 (2015).
83. Bussmann, E., Rudolph, M., Subramania, G.S., Misra, S., Carr, S.M., Langlois, E., Dominguez, J., Pluym, T., Lilly, M.P., Carroll, M.S.: Scanning capacitance microscopy registration of buried atomic-precision donor devices. Nanotechnology. 26, 085701 (2015).
84. Ou, X., Kanungo, P. Das, Kögler, R., Werner, P., Gösele, U., Skorupa, W., Wang, X.: Carrier profiling of individual si nanowires by scanning spreading resistance microscopy. Nano Lett. 10, 171–175 (2010).
85. Eyben, P., Denis, S., Clarysse, T., Vandervorst, W.: Progress towards a physical contact model for scanning spreading resistance microscopy. Mater. Sci. Eng. B. 102, 132–137 (2003).
86. Moth-Poulsen, K., Bjørnholm, T.: Molecular electronics with single molecules in solid-state devices, (2009).
87. Xiang, D., Jeong, H., Lee, T., Mayer, D.: Mechanically controllable break junctions for molecular electronics, (2013).
88. Ajuan, C., Huanli, D., Wenping, H.: Nanogap Electrodes towards Solid State Single-Molecule Transistors. Small. 11, 6115–6141 (2015).
89. Agraït, N.: Quantum properties of atomic-sized conductors. Phys. Rep. 377, 81–279 (2003).
90. Slade, P.G.: No Title. CRC Press (2013).
91. Enachescu, M., van den Oetelaar, R.J.A., Carpick, R.W., Ogletree, D.F., Flipse, C.F.J., Salmeron, M.: Observation of proportionality between friction and contact area at the nanometer scale. Tribol. Lett. 7, 73 (1999).
92. Hu, X., Lee, J., Berman, D., Martini, A.: Substrate effect on electrical conductance

at a nanoasperity-graphene contact. Carbon N. Y. 137, 118–124 (2018).
93. Toler, B.F., Coutu Jr, R.A., McBride, J.W.: A review of micro-contact physics for microelectromechanical systems (MEMS) metal contact switches. J. Micromechanics Microengineering. 23, 103001 (2013).
94. Li, L., Song, W., Zhang, G., Jia, D.: An electrical contact resistance model including roughness effect for a rough MEMS switch. J. Micromechanics Microengineering. 22, 115023 (2012).
95. Zhou, T., Zheng, P., Pandey, S.C., Sundararaman, R., Gall, D.: The electrical resistivity of rough thin films: A model based on electron reflection at discrete step edges. J. Appl. Phys. 123, (2018).
96. Jensen, B.D., Huang, K., Chow, L.L.W., Kurabayashi, K.: Low-force contact heating and softening using micromechanical switches in diffusive-ballistic electron-transport transition. Appl. Phys. Lett. (2005).
97. Rezvanian, O., Zikry, M.A., Brown, C., Krim, J.: Surface roughness, asperity contact and gold RF MEMS switch behavior. J. Micromechanics Microengineering. 17, 2006–2015 (2007).
98. Majumder, S., McGruer, N.E., Adams, G.G., Zavracky, P.M., Morrison, R.H., Krim, J.: Study of contacts in an electrostatically actuated microswitch. Sensors Actuators, A Phys. 93, 19–26 (2001).
99. Brown, C., Rezvanian, O., Zikry, M.A., Krim, J.: Temperature dependence of asperity contact and contact resistance in gold RF MEMS switches. J. Micromechanics Microengineering. 19, (2009).
100. Kogut, L., Komvopoulos, K.: Electrical contact resistance theory for conductive rough surfaces. J. Appl. Phys. 94, 3153–3162 (2003).
101. Kogut, L., Komvopoulos, K.: Electrical contact resistance theory for conductive rough surfaces separated by a thin insulating film. J. Appl. Phys. 95, 576–585 (2004).
102. Coutu, R.A., Reid, J.R., Cortez, R., Strawser, R.E., Kladitis, P.E.: Microswitches with sputtered Au, AuPd, Au-on-AuPt, and AuPtCu alloy electric contacts. IEEE Trans. Components Packag. Technol. 29, 341–349 (2006).
103. Zhou, Z., Nie, W., Xi, Z., Wang, X.: Electrical contact performance of MEMS acceleration switch fabricated by UV-LIGA technology. Microsyst. Technol. 21, 2271–2278 (2015).
104. Valencia, D., Wilson, E., Jiang, Z., Valencia-Zapata, G.A., Wang, K.C., Klimeck, G., Povolotskyi, M.: Grain-Boundary Resistance in Copper Interconnects: From an Atomistic Model to a Neural Network. Phys. Rev. Appl. 9, (2018).
105. Wang, J., Wu, Z., Mao, C., Zhao, Y., Yang, J., Chen, Y.: Effect of electrical contact resistance on measurement of thermal conductivity and wiedemann-franz law for individual metallic nanowires. Sci. Rep. 8, (2018).
106. Oliver, D.J., Maassen, J., El Ouali, M., Paul, W., Hagedorn, T., Miyahara, Y., Qi, Y., Guo, H., Grütter, P.: Conductivity of an atomically defined metallic interface. Proc. Natl. Acad. Sci. U. S. A. 109, 19097–19102 (2012).
107. Streller, F., Wabiszewski, G.E., Carpick, R.W.: Development and Assessment of Next-Generation Nanoelectromechanical Switch Contact Materials*. In: Proceedings from the IEEE Conference on Nanotechnology. pp. 141–145. ,

Toronto, Canada (2014).
108. Yang, F., Carpick, R.W., Srolovitz, D.J.: Mechanisms of Contact, Adhesion, and Failure of Metallic Nanoasperities in the Presence of Adsorbates: Toward Conductive Contact Design. ACS Nano. (2016).
109. Qi, Y., Yang, J., Rappe, A.M.: Theoretical Modeling of Tribochemical Reaction on Pt and Au Contacts: Mechanical Load and Catalysis. ACS Appl. Mater. Interfaces. (2016).
110. Jacobs, T.D.B., Ryan, K.E., Keating, P.L., Grierson, D.S., Lefever, J.A., Turner, K.T., Harrison, J.A., Carpick, R.W.: The Effect of Atomic-Scale Roughness on the Adhesion of Nanoscale Asperities: A Combined Simulation and Experimental Investigation. Tribol. Lett. 50, 81–93 (2013).
111. Vishnubhotla, S.B. Chen, Rimei. Khanal, Subarna. Martini, Ashlie. Jacobs, T.D.B.: Measuring the contact area of platinum nanocontacts at low loads: The effect of reversible plasticity. Submitted. (2018).
112. Foiles, S.M., Baskes, M.I., Daw, M.S.: Embedded-atom-method functions for the fcc metals Cu, Ag, Au, Ni, Pd, Pt, and their alloys. Phys. Rev. B. 33, 7983–7991 (1986).
113. Liem, S.Y., Chan, K.Y.: Effective pairwise potential for simulations of adsorbed platinum. Mol. Phys. 86, 939–949 (1995).
114. Jacobs, T.D.B., Martini, A.: Measuring and Understanding Contact Area at the Nanoscale: A Review. Appl. Mech. Rev. 69, 060802 (2017).
115. Kittel, C.: Introduction to solid state physics. Wiley (1916).
116. Ashcroft, N.W., Mermin, N.D.: Solid State Physics (Holt, Rinehart and Winston, New York, 1976). Google Sch. 403 (2005).
117. Dye, D.H., Ketterson, J.B., Crabtree, G.W.: The Fermi surface of platinum. J. Low Temp. Phys. 30, 813–838 (1978).
118. Mayadas, A.F., Shatzkes, M.: Electrical-resistivity model for polycrystalline films: The case of arbitrary reflection at external surfaces. Phys. Rev. B. 1, 1382–1389 (1970).
119. Argibay, N., Mogonye, J.E., Michael, J.R., Goeke, R.S., Kotula, P.G., Scharf, T.W., Dugger, M.T., Prasad, S. V.: On the thermal stability of physical vapor deposited oxide-hardened nanocrystalline gold thin films. J. Appl. Phys. 117, 145302 (2015).
120. Celano, U., Hantschel, T., Giammaria, G., Chintala, R.C., Conard, T., Bender, H., Vandervorst, W.: Evaluation of the electrical contact area in contact-mode scanning probe microscopy. J. Appl. Phys. 117, 214305 (2015).
121. Pastewka, L., Robbins, M.O.: Contact area of rough spheres: Large scale simulations and simple scaling laws. Appl. Phys. Lett. (2016).
122. Krans, J.M., Muller, C.J., Yanson, I.K., Govaert, T.C.M., Hesper, R., Van Ruitenbeek, J.M.: One-atom point contacts. Phys. Rev. B. 48, 14721–14724 (1993).
123. Smit, R.H.M., Untiedt, C., Yanson, A.I., van Ruitenbeek, J.M.: Common Origin for Surface Reconstruction and the Formation of Chains of Metal Atoms. Phys. Rev. Lett. 87, 266102 (2001).
124. Makk, P., Balogh, Z., Csonka, S., Halbritter, A.: Pulling platinum atomic chains by

carbon monoxide molecules. Nanoscale. 4, 4739–4745 (2012).
125. Yanson, A.I., Bollinger, G.R., van den Brom, H.E., Agraït, N., van Ruitenbeek, J.M.: Formation and manipulation of a metallic wire of single gold atoms. Nat. 395, 783 (1998).
126. Ohnishi, H., Kondo, Y., Takayanagi, K.: Quantized conductance through individual rows of suspended gold atoms. Nature. 395, 780–783 (1998).
127. Simmons, J.G.: Generalized Formula for the Electric Tunnel Effect between Similar Electrodes Separated by a Thin Insulating Film. J. Appl. Phys. (1963).
128. Yoshida, H., Omote, H., Takeda, S.: Oxidation and reduction processes of platinum nanoparticles observed at the atomic scale by environmental transmission electron microscopy. Nanoscale. 6, 13113–13118 (2014).
129. O'Shea, S.J., Atta, R.M., Welland, M.E.: Characterization of tips for conducting atomic force microscopy. Rev. Sci. Instrum. 66, 2508–2512 (1995).
130. Lantz, M., O'Shea, S., Welland, M.: Simultaneous force and conduction measurements in atomic force microscopy. Phys. Rev. B - Condens. Matter Mater. Phys. 56, 15345–15352 (1997).
131. Bratkovsky, A.M., Sutton, A.P., Todorov, T.N.: Conditions for conductance quantization in realistic models of atomic-scale metallic contacts. Phys. Rev. B. 52, 5036–5051 (1995).
132. Olesen, L., Laegsgaard, E., Stensgaard, I., Besenbacher, F., Stoltze, P., Jacobsen, K.W.: Quantized conductance in an atom-sized point contact. Phys. Rev. Lett. 72, 2251–2254 (1994).
133. Chen, L., Lee, H., Guo, Z.J., McGruer, N.E., Gilbert, K.W., Mall, S., Leedy, K.D., Adams, G.G.: Contact resistance study of noble metals and alloy films using a scanning probe microscope test station. J. Appl. Phys. 102, 074910 (2007).
134. Enachescu, M., Carpick, R.W., Ogletree, D.F., Salmeron, M.: The role of contaminants in the variation of adhesion, friction, and electrical conduction properties of carbide-coated scanning probe tips and Pt(111) in ultrahigh vacuum. J. Appl. Phys. 95, 7694–7700 (2004).
135. Sai Bharadwaj Vishnubhotla and Rimei Chen and Subarna R Khanal and Jing Li and Eric A Stach and Ashlie Martini and Tevis D B Jacobs: Quantitative measurement of contact area and electrical transport across platinum nanocontacts for scanning probe microscopy and electrical nanodevices. Nanotechnology. 30, 045705 (2019).
136. Simmons, J.G.: Generalized Formula for the Electric Tunnel Effect between Similar Electrodes Separated by a Thin Insulating Film. J. Appl. Phys. 34, 1793–1803 (1963).
137. Celano, U., Hantschel, T., Giammaria, G., Chintala, R.C., Conard, T., Bender, H., Vandervorst, W.: Evaluation of the electrical contact area in contact-mode scanning probe microscopy. J. Appl. Phys. 117, 214305 (2015).
138. Brown, B.P., Picco, L., Miles, M.J., Faul, C.F.J.: Conductive-AFM Patterning of Organic Semiconductors. Small. 11, 5054–5058 (2015).
139. Yoshida, H., Omote, H., Takeda, S.: Oxidation and reduction processes of platinum nanoparticles observed at the atomic scale by environmental transmission electron microscopy. Nanoscale. 6, 13113–13118 (2014).

140. Erts, D., Olin, H., Ryen, L., Thölén, A.: Maxwell and Sharvin conductance in gold point contacts investigated using TEM-STM. Phys. Rev. B - Condens. Matter Mater. Phys. 61, 12725–12727 (2000).
141. Oliver, D.J., Maassen, J., El Ouali, M., Paul, W., Hagedorn, T., Miyahara, Y., Qi, Y., Guo, H., Grutter, P.: Conductivity of an atomically defined metallic interface. Proc. Natl. Acad. Sci. 109, 19097–19102 (2012).
142. Jiang, Y., Harrison, J.A., David Schall, J., Ryan, K.E., Carpick, R.W., Turner, K.T.: Correcting for Tip Geometry Effects in Molecular Simulations of Single-Asperity Contact. Tribol. Lett. 65, 78 (2017).
143. Fantauzzi, D., Bandlow, J., Sabo, L., Mueller, J.E., van Duin, A.C.T., Jacob, T.: Development of a ReaxFF potential for Pt-O systems describing the energetics and dynamics of Pt-oxide formation. Phys. Chem. Chem. Phys. 16, 23118–23133 (2014).
144. Fantauzzi, D., Krick Calderón, S., Mueller, J.E., Grabau, M., Papp, C., Steinrück, H.P., Senftle, T.P., van Duin, A.C.T., Jacob, T.: Growth of Stable Surface Oxides on Pt(111) at Near-Ambient Pressures. Angew. Chemie - Int. Ed. 56, 2594–2598 (2017).
145. Plimpton, S.: Fast parallel algorithms for short-range molecular dynamics. J. Comput. Phys. 117, 1–19 (1995).
146. Maya, L., Riester, L., Thundat, T., Yust, C.S.: Characterization of sputtered amorphous platinum dioxide films. J. Appl. Phys. 84, 6382–6386 (1998).
147. Maugis, D.: Adhesion of spheres: The JKR-DMT transition using a dugdale model. J. Colloid Interface Sci. 150, 243–269 (1992).
148. Smit, R.H.M., Untiedt, C., Yanson, A.I., Van Ruitenbeek, J.M.: Common origin for surface reconstruction and the formation of chains of metal atoms. Phys. Rev. Lett. 87, 266102-1-266102–4 (2001).
149. Krans, J.M., Muller, C.J., Yanson, I.K., van Ruitenbeek, J.M.: One atom point contacts. Phys. B Condens. Matter. 194–196, 1033–1034 (1994).
150. Smit, R.H.M., Noat, Y., Untiedt, C., Lang, N.D., Van Hemert, M.C., Van Ruitenbeek, J.M.: Measurement of the conductance of a hydrogen molecule. Nature. 419, 906–909 (2002).
151. Strange, M., Thygesen, K.S., Sethna, J.P., Jacobsen, K.W.: Anomalous conductance oscillations and half-metallicity in atomic Ag-O chains. Phys. Rev. Lett. 101, 096804 (2008).
152. Thijssen, W.H.A., Strange, M., aan de Brugh, J.M.J., van Ruitenbeek, J.M.: Formation and properties of metal–oxygen atomic chains. New J. Phys. 10, 033005 (2008).
153. García-Suárez, V.M., Rocha, A.R., Bailey, S.W., Lambert, C.J., Sanvito, S., Ferrer, J.: Single-channel conductance of <math display="inline"> <msub> <mi mathvariant="normal">H</mi> <mn>2</mn> </msub> </math> molecules attached to platinum or palladium electrodes. Phys. Rev. B. 72, 045437 (2005).
154. Thygesen, K.S., Jacobsen, K.W.: Conduction Mechanism in a Molecular Hydrogen Contact. Phys. Rev. Lett. 94, 036807 (2005).
155. Celano, U., Hantschel, T., Giammaria, G., Chintala, R.C., Conard, T., Bender, H., Vandervorst, W.: Evaluation of the electrical contact area in contact-mode

scanning probe microscopy. J. Appl. Phys. 117, 214305 (2015).
156. Holmlin, R.E., Haag, R., Chabinyc, M.L., Ismagilov, R.F., Cohen, A.E., Terfort, A., Rampi, M.A., Whitesides, G.M.: Electron transport through thin organic films in metal-insulator-metal junctions based on self-assembled monolayers. J. Am. Chem. Soc. 123, 5075–5085 (2001).
157. Kergueris, C., Bourgoin, J.P., Esteve, D., Urbina, C., Magoga, M., Joachim, C.: Electron transport through a metal-molecule-metal junction. Phys. Rev. B - Condens. Matter Mater. Phys. 59, 12505–12513 (1999).
158. Bao, J., Macdonald, D.D.: Charge Carrier Tunneling Across the Passive Film on Platinum. ECS Trans. 3, 1–13 (2007).
159. Coutu, R.A., Kladitis, P.E., Leedy, K.D., Crane, R.L.: Selecting metal alloy electric contact materials for MEMS switches. J. Micromechanics Microengineering. 14, 1157–1164 (2004).
160. Lee, H., Coutu, R.A., Mall, S., Leedy, K.D.: Characterization of metal and metal alloy films as contact materials in MEMS switches. J. Micromechanics Microengineering. 16, 557–563 (2006).
161. Chen, L., Lee, H., Guo, Z.J., McGruer, N.E., Gilbert, K.W., Mall, S., Leedy, K.D., Adams, G.G.: Contact resistance study of noble metals and alloy films using a scanning probe microscope test station. J. Appl. Phys. 102, 074910 (2007).
162. Onofrio, N., Guzman, D., Strachan, A.: Atomic origin of ultrafast resistance switching in nanoscale electrometallization cells. Nat. Mater. 14, 440–446 (2015).
163. Israelichvili, J.: Intermolecular and surface forces: revised third edition. Academic press (2011).
164. Gao, H., Yao, H.: Shape insensitive optimal adhesion of nanoscale fibrillar structures. Proc. Natl. Acad. Sci. U. S. A. 101, 7851–7856 (2004).
165. Grierson, D.S., Liu, J., Carpick, R.W., Turner, K.T.: Adhesion of nanoscale asperities with power-law profiles. J. Mech. Phys. Solids. 61, 597–610 (2013).
166. Minor, A.M., Lilleodden, E.T., Jin, M., Stach, E.A., Chrzan, D.C., Morris, J.W.: Room temperature dislocation plasticity in silicon. Philos. Mag. 85, 323–330 (2005).
167. Unertl, W.N.: Implications of contact mechanics models for mechanical properties measurements using scanning force microscopy. J. Vac. Sci. Technol. A Vacuum, Surfaces, Film. 17, 1779 (1999).
168. Espinosa, H.D., Bernal, R.A., Minary-Jolandan, M.: A review of mechanical and electromechanical properties of piezoelectric nanowires, (2012).
169. Yeon, J., Van Duin, A.C.T.: ReaxFF Molecular Dynamics Simulations of Hydroxylation Kinetics for Amorphous and Nano-Silica Structure, and Its Relations with Atomic Strain Energy. J. Phys. Chem. C. 120, 305–317 (2016).
170. Yeon, J., van Duin, A.C.T., Kim, S.H.: Effects of Water on Tribochemical Wear of Silicon Oxide Interface: Molecular Dynamics (MD) Study with Reactive Force Field (ReaxFF). Langmuir. 32, 1018–1026 (2016).
171. Fast parallel algorithms for short-range molecular dynamics. J. Comput. Phys. 117, 1 (1995).
172. Kogut, L., Etsion, I.: Elastic-Plastic Contact Analysis of a Sphere and a Rigid Flat. J. Appl. Mech. 69, 656–657 (2002).

173. Vandeperre, L.J., Giuliani, F., Lloyd, S.J., Clegg, W.J.: The hardness of silicon and germanium. Acta Mater. 55, 6307–6315 (2007).
174. Bernal, R.A., Chen, P., Schall, J.D., Harrison, J.A., Jeng, Y.-R., Carpick, R.W.: Influence of chemical bonding on the variability of diamond-like carbon nanoscale adhesion. Carbon N. Y. 128, 267–276 (2018).
175. Sumant, A. V., Grierson, D.S., Gerbi, J.E., Carlisle, J.A., Auciello, O., Carpick, R.W.: Surface chemistry and bonding configuration of ultrananocrystalline diamond surfaces and their effects on nanotribological properties. Phys. Rev. B. 76, 235429 (2007).
176. Piotrowski, P.L., Cannara, R.J., Gao, G., Urban, J.J., Carpick, R.W., Harrison, J.A.: Atomistic factors governing adhesion between diamond, amorphous carbon and model diamond nanocomposite surfaces. J. Adhes. Sci. Technol. 24, 2471–2498 (2010).
177. Carpick, R.W., Ogletree, D.F., Salmeron, M.: A general equation for fitting contact area and friction vs load measurements. J. Colloid Interface Sci. 211, 395–400 (1999).
178. Katainen, J., Paajanen, M., Ahtola, E., Pore, V., Lahtinen, J.: Adhesion as an interplay between particle size and surface roughness. J. Colloid Interface Sci. 304, 524–529 (2006).
179. Liu, D.L., Martin, J., Burnham, N.A.: Optimal roughness for minimal adhesion. Appl. Phys. Lett. 91, 43107 (2007).
180. Horn, R.G., Israelachvili, J.N., Pribac, F.: Measurement of the deformation and adhesion of solids in contact. J. Colloid Interface Sci. 115, 480–492 (1987).
181. Cross, G.L.W., Schirmeisen, A., Grütter, P., Dürig, U.T.: Plasticity, healing and shakedown in sharp-asperity nanoindentation. Nat. Mater. 5, 370–376 (2006).
182. Vishnubhotla, S.B. Chen, Rimei. Khanal, Subarna. Martini, Ashlie. Jacobs, T.D.B.: Measuring the contact area of platinum nanocontacts at low loads: The effect of reversible plasticity. Nanotechnology. 30, 035704 (2019).
183. Zheng, Z., Yu, J.: Using the Dugdale approximation to match a specific interaction in the adhesive contact of elastic objects. J. Colloid Interface Sci. (2007).
184. Merkle, A.P., Marks, L.D.: Liquid-like tribology of gold studied by in situ TEM. Wear. (2008).
185. Sun, J., He, L., Lo, Y.-C., Xu, T., Bi, H., Sun, L., Zhang, Z., Mao, S.X., Li, J.: Liquid-like pseudoelasticity of sub-10-nm crystalline silver particles. Nat. Mater. (2014).
186. Dos Santos Ferreira, O., Gelinck, E., De Graaf, D., Fischer, H.: Adhesion experiments using an AFM-Parameters of influence. Appl. Surf. Sci. (2010).
187. McMeeking, R.M.: Finite deformation analysis of crack-tip opening in elastic-plastic materials and implications for fracture. J. Mech. Phys. Solids. 25, 357–381 (1977).
188. Guduru, P.R.: Detachment of a rigid solid from an elastic wavy surface: Theory. J. Mech. Phys. Solids. 55, 445–472 (2007).
189. Yang, C., Persson, B.N.J.: Contact mechanics: contact area and interfacial separation from small contact to full contact. J. Phys. Condens. Matter. 20, 215214 (2008).

190. Greenwood, J.A., Williamson, J.B.P.: Contact of Nominally Flat Surfaces. Proc. R. Soc. A Math. Phys. Eng. Sci. 295, 300–319 (1966).
191. Persson, B.N.J.: Elastoplastic contact between randomly rough surfaces. Phys. Rev. Lett. 87, 116101-1-116101–4 (2001).
192. Cohen, D., Kligerman, Y., Etsion, I.: The Effect of Surface Roughness on Static Friction and Junction Growth of an Elastic-Plastic Spherical Contact. J. Tribol. 131, 021404 (2009).
193. Hashiguchi, K., Ozaki, S.: Constitutive equation for friction with transition from static to kinetic friction and recovery of static friction. Int. J. Plast. 24, 2102–2124 (2008).
194. Ranjith, K., Rice, J.R.: Stability of quasi-static slip in a single degree of freedom elastic system with rate and state dependent friction. J. Mech. Phys. Solids. 47, 1207–1218 (1999).
195. Mangolini, F., Rose, F., Hilbert, J., Carpick, R.W.: Thermally induced evolution of hydrogenated amorphous carbon. Appl. Phys. Lett. 103, 161605 (2013).